

NATIONAL UNIVERSITY OF HO CHI MINH CITY
UNIVERSITY OF SCIENCE
FACULTY OF PHYSICS- ENGINEERING PHYSICS

UNDERGRADUATE THESIS

Thesis title:

CALCULATION OF THE LINEAR-ABSORPTION SPECTRUM
OF AN IDEAL TWO-DIMENSIONAL SYSTEM OF MoS_2

Student: Vo Chau Duc Phuong

Supervisor: Dr. Huynh Thanh Duc

Ho Chi Minh city, 2024

NATIONAL UNIVERSITY OF HO CHI MINH CITY
UNIVERSITY OF SCIENCE
FACULTY OF PHYSICS- ENGINEERING PHYSICS

UNDERGRADUATE THESIS

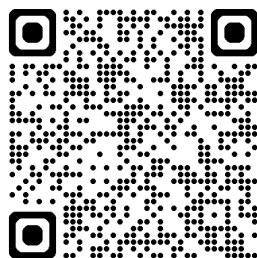
Thesis title:

**Calculation of the Linear-Absorption Spectrum of
an Ideal Two-Dimensional System of MoS₂**

Major code: D440102

Specialization: Theoretical Physics

E-pdf Version:



Student: Vo Chau Duc Phuong
Supervisor: Dr. Huynh Thanh Duc

Ho Chi Minh city, 2024

GUARANTEE

I guarantee to independently conducting the calculation of the linear-absorption spectrum of an ideal two-dimensional system of MoS₂ for my bachelor thesis, under the supervision of Dr. Huynh Thanh Duc, and with guidance from MSc. Le Minh Chau.

The results or products included in this graduation thesis are totally accurate and honest.

STUDENT

(Signature)

Vo Chau Duc Phuong

ACKNOWLEDGMENTS

Even though I still have much more to study to achieve my dream of becoming a physicist, this work marks the first step on my path. I couldn't have completed this work without the guidance of Dr. Huynh Thanh Duc and MSc. Le Minh Chau at the Institute of Physics, Ho Chi Minh City. I am truly grateful to them.

I also want to express my gratitude to Dr. Vu Quang Tuyen, Dr. Vo Quoc Phong, and Dr. Nguyen Huu Nha, three lecturers in the Department of Theoretical Physics. They have guided me throughout my time at the department and at the University of Science, Ho Chi Minh City.

Other thanks go to Pham Nhat Minh, Le Huu Thong, Le Thi Lien, Kien Le, and Phan Anh Luan (Luancio)... I had multiple interesting discussions for a better understanding of my and their research interest.

Contents

1	Introduction	1
2	Theory	4
2.1	Tight-Binding Theory	4
2.2	Three Band Tight-Binding Model	5
2.3	System Hamiltonian	8
2.3.1	Hamiltonian In First Quantization	8
2.3.2	Hamiltonian In Second Quantization	9
2.4	Semiconductor Bloch Equations	11
2.5	Polarization Density	12
3	Numerical Methods	14
3.1	Numerical Evaluation of The Sum over k	14
3.2	Cut-off K -point Technique	15
3.3	Absorption Coefficient	16
4	Results and Discussion	17
5	Conclusion and Further Research	21
	Appendices	22
A	Coulomb matrix elements	22
B	Equation of Motion	24
C	Dipole Matrix Elements	26

List of Acronyms

TMDs transition metal dichacolgenides	vi
LAS linear absorption spectrum	vi
BPV bulk photovoltaic	1
2D two-dimensional	1
BZ Brillouin zone	2
SBE semiconductor Bloch equations	2
LCAO linear combination of atomic orbitals	4
TNN three-band third-nearest-neighbor-model	6
SOC spin orbit coupling	6
LDA local-density approximation	7
VG velocity gauge	9
HHG high harmonic generation	21
HSG high-order sideband generation	21

List of Figures

1	TMD structure and its first Brillouin zone	5
2	Band structure of MoS_2 material along ΓK direction	8
3	Rhombus primitive unit cell in comparison with hexagon primitive unit cell (the first Brillouin zone)	14
4	New basis Based on the rhombus unit vectors	15
5	k-radius show the cutoff circle around K' points	16
6	Electric field on Ox direction and its Fourier Transform	17
7	Absorption spectrum of MoS_2	18
8	Absorption spectrum with difference T_2	19
9	Absorption spectrum with difference dielectric ε and without Coulomb interaction	20
10	Absorption spectrum with difference number of k-points	20

List of Tables

1	Fitting parameters in three-band tight-binding model for MoS_2	7
2	Exciton binding energy with difference ε	18

Thesis Information

Name of Thesis: Calculation of the Linear-Absorption Spectrum of MoS₂

Major: Physics

Specialty: Theoretical Physics

Name of Student: Vo Chau Duc Phuong

Student ID: 20130008

Academic Year: 2020

Supervisor: Dr. Huynh Thanh Duc

Abstract

transition metal dichalcogenides (TMDs) are promising semiconductors due to their extraordinary electronic and optoelectronic properties. Before calculating the nonlinear optical properties of this material, we need to calculate the linear absorption spectrum. In monolayer TMD, the Coulomb interaction heavily influences the increase in exciton binding energies. Therefore, the independent electron approximation model is unreliable for simulating the experiment, especially in low-dimensional systems. In this work, we use a minimum three-band tight-binding Hamiltonian for the band structure calculation and the semiconductor Bloch equations to model the response of electron density in material to a laser over time to calculate the linear absorption spectrum (LAS) and extract the exciton binding energy from it.

Novelty Of Thesis

Our calculation on exciton binding energy (0.242 eV) based on this model proves to agree with the experiment. It proves to be more accurate than some previous theories, which predicted exciton binding energy too large (0.5-1 eV).

Applications/ Applicability/ Perspective

From this work, we can use it to calculate other linear- and nonlinear-effects that are affected by exciton binding energy such as photo-current, high harmonic generation, and high-order sideband generation. For further work, we can increase the density of the k-point for better convergence results. Considering the shield coulomb interaction when increasing the density of electrons on the conduction bands when excess of the low excitation limit for full absorption spectra.

SUPERVISOR

STUDENT

**CERTIFICATION
UNIVERSITY OF SCIENCE
PRESIDENT**

1 Introduction

When exploring the properties of a material, the linear absorption spectrum is a crucial tool. This spectrum provides valuable insights into the material's electronic structure by precisely measuring the energy of absorbed photons. This analysis helps us understand the material's energy levels, transitions between states, and the nature of electron excitation. By examining the absorption peaks and bands, we can calculate important coefficients such as absorbance and extinction coefficients, which are vital in various scientific and industrial applications.

The photovoltaic effect is the generation of a photo-current and voltage in a material under illumination, caused by charge separation involving two or more material components¹. In conventional solar cells that use a p-n junction for photo-electric conversion, the maximum efficiency is limited to about 33% when the band gap of the material is 1.4 eV². However, the bulk photovoltaic (BPV) effect, which is a second-order non-linear optical phenomenon occurring when non-centrosymmetric materials are illuminated by a laser, is expected to surpass the Shockley-Queisser limit. Under linearly polarized laser illumination, electrons transition from valence bands to conduction bands, creating a shift current by changing the electron's center of symmetry. When circularly polarized lasers are used, only electrons with a specific spin orientation, dependent on the laser's circular direction, are stimulated, creating an injection current. When accounting for electron-electron Coulomb interactions, the asymmetry of the Coulomb interaction results in an asymmetry of the electron density distribution, which creates a ballistic current. The complexity of including the electron-electron Coulomb interaction sometimes causes it to be ignored, but this contribution is not small³.

The researchers have dedicated many years to studying Graphene, with hopes that it could potentially serve as the new silicon, enabling the continuation of Moore's law on the CPU chip dice. However, in recent years, the number of papers on Graphene properties has reached thousands yearly, indicating that research on 'simple graphene' has peaked⁴. Therefore, the researchers shifted their focus from working solely with Graphene to exploring applications and other two-dimensional materials. Atomically thin two-dimensional (2D) forms of layered TMD have recently gained significant scientific and technological interest since the first five years of the Graphene boom^{4;5}.

TMD has the chemical composition MX_2 , so it has a wide range of materials. They include both metals and semiconductors, for example NbS₂, NbSe₂, TaS₂, TaSe₂, β -MoT₂ and Td-WTe₂ are bulk metals while the ReS₂, ZrS₂, MoS₂, WS₂, MoSe₂, WSe₂ and α -MoTe₂ are semiconductors. The structure of TMD consists of multiple monolayers bonded by van der Waals forces, with in-plane stability ensured by strong covalent bonds.

TMD exhibits non-centrosymmetry in monolayers form, resulting in unique properties in electronic, spintronics, optoelectronics, superconduction, and valleytronic applications^{6;7}.

Among various TMD, the group-VIB ($M = \text{Mo, W}$; $X = \text{S, Se}$) is stable in both mono- and few-layers in the air at room temperature⁴. Additionally, significant spin-orbit coupling in TMD creates a considerable split in the band structure valley. These two-dimensional semiconductors have a direct band gap in the visible frequency range, stable and excellent mobility at room temperature^{1;5}, and promise to become a good candidate for electronic and optoelectronic applications. Its nanotube structure has been researched and also shows its potential to become the new solar cell material^{1;8-10}.

The low dimension system causes the reduced screening of Coulomb interaction outside the monolayer's plane, resulting in larger exciton binding energies^{11;12}. These binding energies are notably higher than those observed in typical III-V materials, implying that many-body interactions play a key role in determining the electronic and optical properties of these materials. In some previous work, only the nearly free electron approximation has been taken into account and did not give good accuracy on the results as the key role of many-body interactions in the system in simulating the photoelectric currents. Furthermore, previous theoretical works have predicted the binding energy too large¹³⁻¹⁶ when compared with experiment¹² and other more accurate theoretical works^{11;12;17}. Therefore, this thesis will focus on calculating the exciton binding energy through the absorption spectrum to fit the results with experiments and other theoretical work.

In our current research, our main objective is to identify the appropriate model for estimating the exciton binding energy while aligning with experimental data. The key challenge is to identify a model that balances simplicity and accuracy. Our primary focus is on investigating the properties of TMD. Several models, such as ab initio calculations^{11;13-16} and parabola approximation^{18;19}, have been developed and employed to simulate the band structure. It is important to note that these models have limitations as they can only be calculated around highly symmetric points and not across the entire Brillouin zone (BZ). In our study, we are using a three-band tight-binding model to calculate properties across the entire BZ, which should give us results that better match experimental data.

In this work, we use the minimal three-band tight-binding Hamiltonian²⁰ to calculate the band structure by determining the eigenvalues at each k-point. The momentum matrix for the velocity gauge matrix will be calculated using finite differentiation and then utilized to compute the dipole matrix. We plan to solve the semiconductor Bloch equations (SBE) using the Runge-Kutta 4th-order method to numerically find the time-dependent density evolution. Based on this density, we can derive the polarization, current density, and other measurable physical observations. After obtaining the polarization density, we will perform a Fourier transform to obtain the absorption spectrum.

In our analysis, we concentrate on the low excitation regime to examine the linear absorption spectra. We were able to concentrate on scenarios where the electron density in the conduction bands is significantly lower than that in the valence bands. The results show a

significant exciton binding energy, which closely matched both experimental measurements and theoretical expectations. These discoveries allow us to predict the existence of smaller excitons and use the binding energy to investigate other effects influenced by the Coulomb interaction.

The main content of this thesis included:

- Briefing the tight-binding theory with some important approximations such as independent electron approximation and tightly bound electron approximation. Then the electron wave functions will be constructed based on the linear combination of atomic orbitals. Introducing the parameters of this model: hopping energies and overlap density. In our concern with MoS₂, the parameters of the tight-binding model will be obtained from the three-band tight-binding model presented in Ref.²⁰. This model is chosen to fit with the band structure obtained from ab initio calculation in the entire first Brillouin zone. Deriving the Hamiltonian for a multi-body electron system in interaction with an external electromagnetic field in velocity gauge, the semiconductor Bloch equations describe the dynamic optoelectronic response that includes the electron-electron Coulomb interaction in the Hartree-Fock approximation.
- Introducing the formulas to calculate the dipole matrix and microscopic polarization density, the rhombus basis, and the basis transformation between rectangular and rhombus basis. Presenting the cut-off technique to reduce workloads in many-body interaction calculation when increasing the number of k-points in a discrete k-grid. Introducing parameters for the linear absorption spectrum formula, parameters for the external field, and its Fourier transform.
- Results and discussion on the aligning between numerical results and measurement. Conclusion on the exciton binding energy and discussion on the relation between dielectric, relaxation, and density of k-point in k-grid and the absorption spectrum. Further discussion on the disadvantages encountered in the calculation process and suggesting the overcome path.

2 Theory

2.1 Tight-Binding Theory

The Hamiltonian of a system, when Coulomb interaction between electrons is not taken into account, is the sum of independent electron Hamiltonians:

$$H = \sum_i H_{1e}(\mathbf{r}_i), \quad (1)$$

in which, $H_{1e}(\mathbf{r}_a)$ is the single electron Hamiltonian. In the independent electron approximation, the stationary state of an electron in a solid is presented by the one-particle time-independent Schrödinger equation:

$$H_{1e}\psi_{\lambda\mathbf{k}}(\mathbf{r}) = \left(-\frac{\hbar^2\nabla^2}{2m} + V_0(\mathbf{r}) \right) \psi_{\lambda\mathbf{k}}(\mathbf{r}) = \varepsilon_{\lambda}(\mathbf{k})\psi_{\lambda\mathbf{k}}(\mathbf{r}), \quad (2)$$

where V_0 is the periodic potential of ions, $V_0(\mathbf{r}) = V_0(\mathbf{r} + \mathbf{R}_n)$, in which \mathbf{R}_n is a lattice vector. $\psi_{\lambda\mathbf{k}}(\mathbf{r})$ and $\varepsilon_{\lambda}(\mathbf{k})$ are respectively the wave function and energy of electron in band λ with wave vector \mathbf{k} . The electrons are tightly bound to the atom to which they belong and have limited interaction with surrounding atoms. Therefore, the wave function of an electron will have the similar form of well known atomic orbital and we can describe it in the form of linear combination of atomic orbitals (LCAO):

$$\psi(\mathbf{r}) = \sum_{n=1}^N \sum_{c=1}^{N_c} \sum_{\alpha=1}^{N_{orb}} c_{\alpha c}(\mathbf{R}_n) \phi_{\alpha}(\mathbf{r} - \mathbf{R}_n - \mathbf{r}_c). \quad (3)$$

Here, ϕ_{α} is orbital wave function of an atomic, \mathbf{R}_n is position of Bravais unit cell, \mathbf{r}_c is relative position of the atoms in that cell, N_{orb} is number of orbitals of an atom, N_c is number of atoms in a unit cell, and N is the number of unit cells in the lattice. Based on LCAO wave function, we can construct the Bloch wave function in the following form:

$$\psi_{\mathbf{k}}(\mathbf{r}) = \sum_{c=1}^{N_c} \sum_{\alpha=1}^{N_{orb}} C_{\alpha c}(\mathbf{k}) \sum_{n=1}^N e^{i\mathbf{k}(\mathbf{R}_n + \mathbf{r}_c)} \phi_{\alpha}(\mathbf{r} - \mathbf{R}_n - \mathbf{r}_c) \quad (4)$$

This wave function satisfies the Bloch theorem. Substituting Eq. (4) into Eq. (2) then multiplying with $e^{i\mathbf{k}\mathbf{r}_{c'}} \phi_{\alpha'}^*(\mathbf{r} - \mathbf{r}_{c'})$ on the left, and taking the integral over \mathbf{r} , we obtain:

$$\sum_{c=1}^{N_c} \sum_{\alpha=1}^{N_{orb}} (H_{\alpha'c',\alpha c}(\mathbf{k}) - \varepsilon(\mathbf{k}) S_{\alpha'c',\alpha c}(\mathbf{k})) C_{\alpha c}(\mathbf{k}) = 0, \quad (5)$$

where

$$H_{\alpha'c',\alpha c}(\mathbf{k}) = \sum_{n=1}^N e^{i\mathbf{k}(\mathbf{R}_n + \mathbf{r}_c - \mathbf{r}_{c'})} \int d\mathbf{r} \phi_{\alpha'}^*(\mathbf{r} - \mathbf{r}_{c'}) H_{1e} \phi_{\alpha}(\mathbf{r} - \mathbf{R}_n - \mathbf{r}_c), \quad (6)$$

$$S_{\alpha'c',\alpha c}(\mathbf{k}) = \sum_{n=1}^N e^{i\mathbf{k}(\mathbf{R}_n + \mathbf{r}_c - \mathbf{r}_{c'})} \int d\mathbf{r} \phi_{\alpha'}^*(\mathbf{r} - \mathbf{r}_{c'}) \phi_{\alpha}(\mathbf{r} - \mathbf{R}_n - \mathbf{r}_c) \quad (7)$$

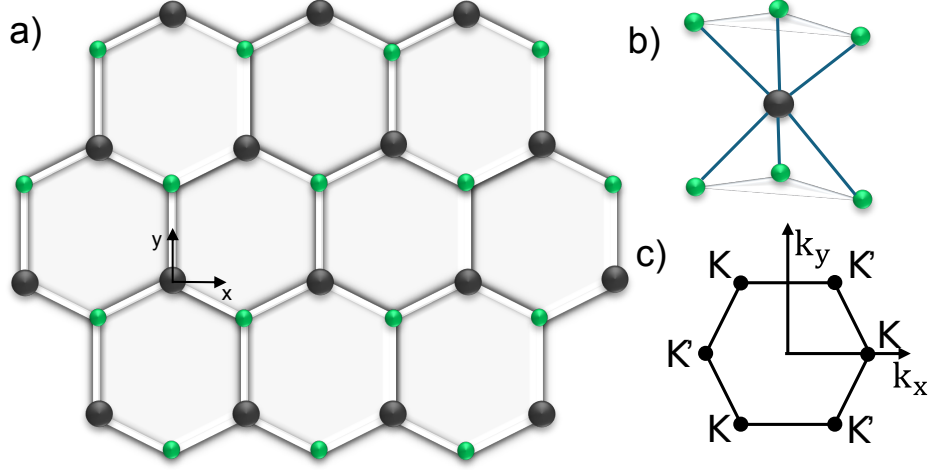


Figure 1: (a) Top view of monolayer MX_2 . The large sphere is M atom and the small sphere is X atom. (b) sideview of monolayer MX_2 . (c) The first Brillouin zone and high symmetry points in two dimensional k -space.

are the Hamiltonian matrix and overlap integral, respectively. By solving Eq. (5) at several k -points, we will have the wave functions and band structure $\varepsilon_\lambda(\mathbf{k})$. In the tight-binding theory, these integrals are given as semi-empirical parameters.

2.2 Three Band Tight-Binding Model

MX_2 monolayers with the crystal structure illustrated in Fig. 1 have the symmetry of D_{3h} point group. From previous ab initio calculations^{21–25}, it is shown that the electron states near the band edges of MX_2 are mainly contributed from the d orbitals of M atom, including d_{z^2} , d_{xy} and $d_{x^2-y^2}$ orbitals. In Ref.²⁰, G-B Liu et al. construct a tight-binding model using the minimal set of the above three orbitals as a basis. This model is called the three-band tight-binding model. Three orbital wave functions of M atom are denoted as:

$$|\phi_1\rangle = d_{z^2}, \quad |\phi_2\rangle = d_{xy}, \quad |\phi_3\rangle = d_{x^2-y^2}. \quad (8)$$

Since the basis consists only of the orbitals of atom M and not of atom X , we ignore the sum over the relative position of the atom \mathbf{r}_c in the unit cell in Eq. (4). Ignoring the wave function overlap between atoms and using the orthogonality of basis functions we have

$$S_{\alpha,\alpha'}(\mathbf{k}) = \delta_{\alpha\alpha'}.$$

The Hamiltonian matrix elements Eq.(6) between the atomic orbitals $|\phi_\mu\rangle$ at the origin and $|\phi_{\mu'}\rangle$ at the lattice vector \mathbf{R} can be obtained as:

$$H_{\mu\mu'}(\mathbf{k}) = \sum_{\mathbf{R}} e^{i\mathbf{k}\cdot\mathbf{R}} \langle \phi_\mu(\mathbf{r}) | \hat{H} | \phi_{\mu'}(\mathbf{r} - \mathbf{R}) \rangle.$$

Three-bands tight-binding model that takes into account the nearest neighbor hopping is call the three-band nearest-neighbor model. This model agrees well with the ab initio calculation for the bandstructure near the band edge, but they significantly deviate in other regions. The three-band third-nearest-neighbor-model (TNN) is the three-band tight-binding model taking into account up to the third nearest hoppings. Confined by the symmetry of the system, the three-band third-nearest-neighbor tight-binding Hamiltonian has the form²⁰:

$$H^{TNN}(\mathbf{k}) = \begin{pmatrix} V_0 & V_1 & V_2 \\ V_1^* & V_{11} & V_{12} \\ V_2^* & V_{12}^* & V_{22} \end{pmatrix}, \quad (9)$$

where

$$\begin{aligned} V_0 &= \varepsilon_1 + 2t_0(2\cos\alpha\cos\beta + \cos 2\alpha) + 2r_0(2\cos 3\alpha\cos\beta + \cos 2\beta), \\ \text{Re}[V_1] &= -2\sqrt{3}t_2\sin\alpha\sin\beta + 2(r_1 + r_2)\sin 3\alpha\sin\beta - 2\sqrt{3}u_2\sin 2\alpha\sin 2\beta, \\ \text{Im}[V_1] &= 2t_1\sin\alpha(2\cos\alpha + \cos\beta) + 2(r_1 - r_2)\sin 3\alpha\cos\beta + 2u_1\sin 2\alpha(2\cos 2\alpha + \cos 2\beta) \\ \text{Re}[V_2] &= 2t_2(\cos 2\alpha - \cos\alpha\cos\beta) - \frac{2}{\sqrt{3}}(r_1 + r_2)(\cos 3\alpha\cos\beta - \cos 2\beta) \\ &\quad + 2u_2(\cos 4\alpha - \cos 2\alpha\cos 2\beta), \\ \text{Im}[V_2] &= 2\sqrt{3}t_1\cos\alpha\sin\beta + \frac{2}{\sqrt{3}}\sin\beta(r_1 - r_2)(\cos 3\alpha + 2\cos\beta), \\ V_{11} &= \varepsilon_2 + (t_{11} + 3t_{22})\cos\alpha\cos\beta + 2t_{11}\cos 2\alpha + 4r_{11}\cos 3\alpha\cos\beta \\ &\quad + 2(r_{11} + \sqrt{3}r_{12})\cos 2\beta + (u_{11} + 3u_{22})\cos 2\alpha\cos 2\beta + 2u_{11}\cos 4\alpha, \\ \text{Re}(V_{12}) &= \sqrt{3}(t_{22} - t_{11})\sin\alpha\sin\beta + 4r_{12}\sin 3\alpha\sin\beta + \sqrt{3}(u_{22} - u_{11})\sin 2\alpha\sin 2\beta, \\ \text{Im}[V_{12}] &= 4t_{12}\sin\alpha(\cos\alpha - \cos\beta) + 4u_{12}\sin 2\alpha(\cos 2\alpha - \cos 2\beta), \\ V_{22} &= \varepsilon_2 + (3t_{11} + t_{22})\cos\alpha\cos\beta + 2t_{22}\cos 2\alpha + 2r_{11}(2\cos 3\alpha\cos\beta + \cos 2\beta) \\ &\quad + \frac{2}{\sqrt{3}}r_{12}(4\cos 3\alpha\cos\beta - \cos 2\beta) + (3u_{11} + u_{22})\cos 2\alpha\cos 2\beta + 2u_{22}\cos 4\alpha, \end{aligned}$$

and

$$(\alpha, \beta) = \left(\frac{1}{2}k_x a, \frac{\sqrt{3}}{2}k_y a\right), \quad (10)$$

11-additional parameters shown in table 1 are obtained by fitting with ab initio calculation results. Due to the heavy mass of the transition-metal atom M, its spin orbit coupling (SOC) can be large. For simplicity, only the on-site contribution, namely, the $\mathbf{L}\cdot\mathbf{S}$ term from M atoms, is considered. Using the basis $\{|d_{z^2}, \uparrow\rangle, |d_{xy}, \uparrow\rangle, |d_{x^2-y^2}, \uparrow\rangle, |d_{z^2}, \downarrow\rangle, |d_{xy}, \downarrow\rangle, |d_{x^2-y^2}, \downarrow\rangle\}$, the contribution of SOC to the Hamiltonian can be written as

$$H' = \lambda \mathbf{L}\cdot\mathbf{S} = \frac{\lambda}{2} \begin{pmatrix} L_z & 0 \\ 0 & -L_z \end{pmatrix}. \quad (11)$$

ε_1	ε_2	t_0	t_1	t_2	t_{11}	t_{12}	t_{22}	r_0	r_1
r_2	r_{11}	r_{12}	u_0	u_1	u_2	u_{11}	u_{12}	u_{22}	λ
0.820	1.931	-0.176	-0.101	0.531	0.084	0.169	0.070	0.070	-0.252
0.084	0.019	0.093	-0.043	0.047	0.005	0.304	-0.192	-0.162	0.073

Table 1: Fitting parameters in three-band tight-binding model for local-density approximation (LDA) cases for MoS_2 .²⁰

In which,

$$L_z = \begin{pmatrix} 0 & 0 & 0 \\ 0 & 0 & 2i \\ 0 & -2i & 0 \end{pmatrix}, \quad (12)$$

is the matrix of \hat{L}_z (z component of the orbital angular momentum) in basis of d_{z^2} , d_{xy} and $d_{x^2-y^2}$, and λ is characterized for the strength of the SOC. Under these bases, the matrix elements of \hat{L}_x and \hat{L}_y are all zeros. Therefore the Hamiltonian with SOC has the form:

$$H(\mathbf{k}) = H_{SOC}(\mathbf{k}) = I_2 \otimes H^{TNN}(\mathbf{k}) + H' = \begin{bmatrix} H(\mathbf{k}) + \frac{\lambda}{2}L_z & 0 \\ 0 & H_0(\mathbf{k}) - \frac{\lambda}{2}L_z \end{bmatrix}. \quad (13)$$

To obtain the band structure, the eigenvalue of the Hamiltonian needs to be found at each k point across the entire BZ. The band structure diagram in Figure 2 illustrates the significant splitting ($\Delta_{SOC}^\lambda = 2\lambda = 146 \text{ meV}$) of the valence bands at the K and K' points of MoS_2 caused by the SOC.

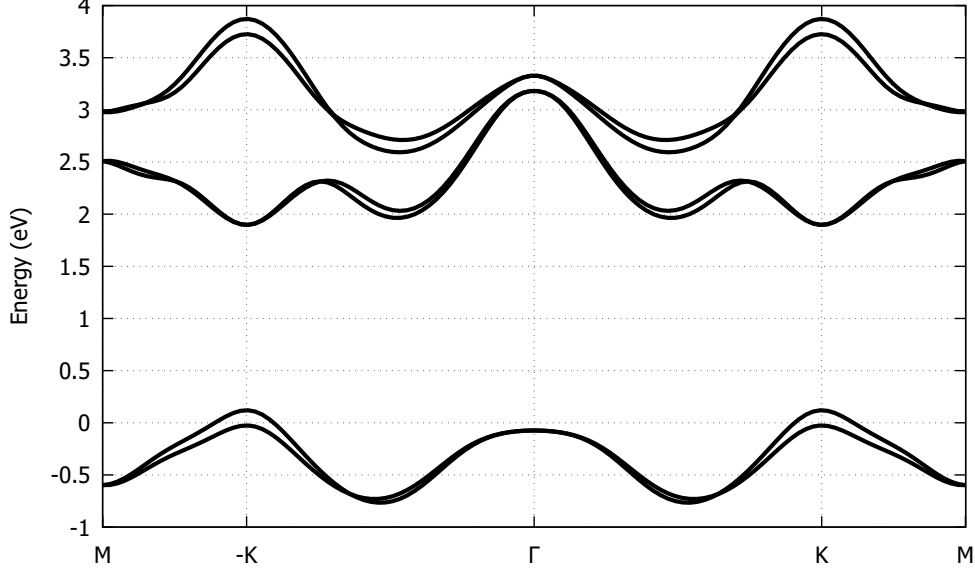


Figure 2: Band structure of monolayer-MoS₂ along Γ K direction, SOC causes huge spin splittings in band-structure at K and $-K$ points.

2.3 System Hamiltonian

2.3.1 Hamiltonian In First Quantization

Accounting the Coulomb interaction between electrons in the many-body system, the system Hamiltonian can be written in form:

$$H = H^0 + H^{Coul} = \sum_i H_{1e}(\mathbf{r}_i) + \frac{1}{2} \sum_{i,j} H^{e-e}(\mathbf{r}_i, \mathbf{r}_j), \quad (14)$$

where H_{1e} is the single electron Hamiltonian:

$$H_{1e}(\mathbf{r}_i) = \frac{\mathbf{P}_i^2}{2m} + V_0(\mathbf{r}_i). \quad (15)$$

In which $V_0(\mathbf{r})$ is interaction between electron and ions. The Coulomb interaction between two electrons can be described by:

$$H^{e-e}(\mathbf{r}_i, \mathbf{r}_j) \equiv V_{e-e}(\mathbf{r}_i, \mathbf{r}_j) = \frac{1}{4\pi\epsilon\epsilon_0} \frac{e^2}{|\mathbf{r}_i - \mathbf{r}_j|}, \quad (16)$$

in which the ϵ_0 is the vacuum permittivity, ϵ is relative permittivity. In the present of an external electromagnetic field, the Hamiltonian for an electron in the independent electron approximation takes the form:

$$H_{1e} = \frac{(\mathbf{p} + e\mathbf{A})^2}{2m} + V_0(\mathbf{r}) - e\phi, \quad (17)$$

in which, \mathbf{A} is vector potential and ϕ is scalar potential. With $\mathbf{p} = -i\hbar\nabla$, we expand $(\mathbf{p} + e\mathbf{A})^2 = \mathbf{p}^2 + 2e\mathbf{A}\mathbf{p} + ei\hbar\nabla(\mathbf{A}) + (e\mathbf{A})^2$. We have $\nabla \cdot (\mathbf{A}) = 0$ due to Coulomb gauge, so

the Eq. (17) becomes

$$H_{1e} = H_{1e}^0 + \frac{e}{m} \mathbf{A} \cdot \mathbf{p} + \frac{e^2 \mathbf{A}^2}{2m} - e\phi, \quad (18)$$

where the H_{1e}^0 is stationary Hamiltonian of a single electron:

$$H_{1e}^0 = \frac{\mathbf{p}^2}{2m} + V_0(\mathbf{r}), \quad (19)$$

the rest in Eq. (18) shall be defined as the light-matter interaction Hamiltonian H_{1e}^{e-L} :

$$H_{1e}^{e-L} = \frac{e}{m} \mathbf{A} \cdot \mathbf{p} - e\phi + \frac{e^2 \mathbf{A}^2}{2m}. \quad (20)$$

When we choose gauge $\phi = 0$, relation between \mathbf{A} and ϕ becomes:

$$\mathbf{E} = -\nabla\phi - \frac{\partial \mathbf{A}}{\partial t} = -\frac{\partial \mathbf{A}}{\partial t}, \quad (21)$$

$$\mathbf{A}(\mathbf{r}, t) = -\int_{-\infty}^t dt' \mathbf{E}(\mathbf{r}, t'). \quad (22)$$

Substituting $\phi = 0$ into Eq. (18), one has

$$H_{1e}^{VG} = H_{1e}^0 + \frac{e}{m} \mathbf{A} \cdot \mathbf{p} + \frac{e^2 \mathbf{A}^2}{2m}. \quad (23)$$

From the definition of the velocity operator $\mathbf{v} = \frac{i}{\hbar} [H_{1e}, \mathbf{r}] = \frac{\mathbf{p} + e\mathbf{A}}{m}$, H_{1e}^{VG} can be written in the form

$$H_{1e}^{VG} = H_{1e}^0 + e\mathbf{A} \cdot \mathbf{v} - \frac{e^2 \mathbf{A}^2}{2m}. \quad (24)$$

In Eq. (24), the second term consists of the external field \mathbf{A} multiplied by a quantity with the unit of velocity. Thus, the gauge $\phi = 0$ that we have chosen to fix the relation between \mathbf{A} and \mathbf{E} is called "the velocity gauge (VG)". In the VG, the light-matter interaction Hamiltonian (20) takes the form:

$$H_{1e}^{e-L} = \frac{e}{m} \mathbf{A} \cdot \mathbf{p} + \frac{e^2 \mathbf{A}^2}{2m}. \quad (25)$$

Combining Eqs. (19), (16), and (25), we obtain the many-body Hamiltonian describing the system of electrons interacting with an external electromagnetic field:

$$H = \sum_i H_{1e}^0(\mathbf{r}_i) + \sum_i H_{1e}^{e-L}(\mathbf{r}_i, t) + \frac{1}{2} \sum_{\mathbf{r}_i, \mathbf{r}_j} H^{e-e}(\mathbf{r}_i, \mathbf{r}_j). \quad (26)$$

2.3.2 Hamiltonian In Second Quantization

From Eq. (26), the second quantized Hamiltonian in Bloch basis $\{|\psi_{\lambda\mathbf{k}}\rangle\}$ has the form:

$$\begin{aligned} \hat{H} &= \hat{H}^0 + \hat{H}^{e-L} + \hat{H}^{e-e}, \\ \hat{H}^0 &= \sum_{\lambda\lambda'\mathbf{k}\mathbf{k}'} \langle \psi_{\lambda\mathbf{k}} | H_{1e}^0(\mathbf{r}) | \psi_{\lambda'\mathbf{k}'} \rangle c_{\lambda\mathbf{k}}^\dagger c_{\lambda'\mathbf{k}'}, \\ \hat{H}^{e-L} &= \sum_{\lambda\lambda'\mathbf{k}\mathbf{k}'} \langle \psi_{\lambda\mathbf{k}} | H^{e-L}(\mathbf{r}) | \psi_{\lambda'\mathbf{k}'} \rangle c_{\lambda\mathbf{k}}^\dagger c_{\lambda'\mathbf{k}'}, \\ \hat{H}^{e-e} &= \frac{1}{2} \sum_{\mathbf{k}, \mathbf{k}', \mathbf{q}} \sum_{\alpha\beta\gamma\delta} \langle \psi_{\alpha\mathbf{k}} + \mathbf{q} \psi_{\beta\mathbf{k}'-\mathbf{q}} | V_{e-e} | \psi_{\gamma\mathbf{k}'} \psi_{\delta\mathbf{k}} \rangle c_{\alpha, \mathbf{k}+\mathbf{q}}^\dagger c_{\beta, \mathbf{k}'-\mathbf{q}}^\dagger c_{\gamma, \mathbf{k}} c_{\delta, \mathbf{k}'}, \end{aligned} \quad (27)$$

in which the basis is orthonormal: $\langle \psi_{\lambda\mathbf{k}} | \psi_{\lambda'\mathbf{k}'} \rangle = \delta_{\lambda\lambda'} \delta_{\mathbf{k}\mathbf{k}'}$, and the creation and annihilation operators satisfy the anti-commutator relations:

$$\{c_{\lambda,\mathbf{k}}, c_{\lambda',\mathbf{k}'}\} = \{c_{\lambda,\mathbf{k}}^\dagger, c_{\lambda',\mathbf{k}'}^\dagger\} = 0, \quad \{c_{\lambda,\mathbf{k}}, c_{\lambda',\mathbf{k}'}^\dagger\} = \delta_{\lambda,\lambda'} \delta_{\mathbf{k},\mathbf{k}'}. \quad (28)$$

If we choose the basis to be a set of eigenvectors of H_{1e}^0 then H^0 becomes:

$$\hat{H}^0 = \sum_{\lambda\mathbf{k}} \varepsilon_\lambda(\mathbf{k}) c_{\lambda\mathbf{k}}^\dagger c_{\lambda\mathbf{k}}. \quad (29)$$

It is worth noting that the eigenvector of H_{1e}^0 does not satisfy the orthonormality in general but only satisfies it if \mathbf{k} and \mathbf{k}' are small. In VG, the elements of interaction Hamiltonian matrix $\langle \psi_{\lambda\mathbf{k}} | H^{e-L}(\mathbf{r}, t) | \psi_{\lambda'\mathbf{k}'} \rangle$ is:

$$\begin{aligned} \langle \psi_{\lambda\mathbf{k}} | H^{e-L}(\mathbf{r}, t) | \psi_{\lambda'\mathbf{k}'} \rangle &= \langle \psi_{\lambda\mathbf{k}} | \frac{e}{m} \mathbf{A}(\mathbf{r}, t) \cdot \mathbf{p} | \psi_{\lambda'\mathbf{k}'} \rangle + \frac{e^2 A^2}{2m} \delta_{\lambda\lambda'} \delta_{\mathbf{k}\mathbf{k}'} \\ &\approx \frac{e}{m} \mathbf{A}(t) \cdot \langle \psi_{\lambda\mathbf{k}} | \mathbf{p} | \psi_{\lambda'\mathbf{k}'} \rangle + \frac{e^2 A^2}{2m} \delta_{\lambda\lambda'} \delta_{\mathbf{k}\mathbf{k}'}, \end{aligned} \quad (30)$$

where

$$\begin{aligned} \langle \psi_{\lambda\mathbf{k}} | \mathbf{p} | \psi_{\lambda'\mathbf{k}'} \rangle &= \int \frac{d^3r}{V} e^{-i\mathbf{k}\cdot\mathbf{r}} u_{\lambda\mathbf{k}}^*(\mathbf{r}) \hat{\mathbf{p}}(e^{i\mathbf{k}'\cdot\mathbf{r}} u_{\lambda'\mathbf{k}'}(\mathbf{r})) \\ &= \frac{1}{N} \sum_i e^{i(\mathbf{k}'-\mathbf{k})\mathbf{R}_i} \int_{V_{Cell}} \frac{d^3r}{V_{Cell}} u_{\lambda\mathbf{k}}^*(\mathbf{r}) e^{-i\mathbf{k}\mathbf{r}} \hat{\mathbf{p}} e^{i\mathbf{k}\mathbf{r}} u_{\lambda'\mathbf{k}'}(\mathbf{r}). \end{aligned} \quad (31)$$

using relation $\sum_i e^{i(\mathbf{k}'-\mathbf{k})\mathbf{R}_i} = N \delta_{\mathbf{k}',\mathbf{k}}$. Eq. (31) becomes

$$\langle \psi_{\lambda\mathbf{k}} | \mathbf{p} | \psi_{\lambda'\mathbf{k}'} \rangle \approx \mathbf{p}_{\lambda\lambda'}(\mathbf{k}) \delta_{\mathbf{k},\mathbf{k}'}. \quad (32)$$

In which,

$$\mathbf{p}_{\lambda\lambda'}(\mathbf{k}) = \langle u_{\lambda\mathbf{k}} | \mathbf{p}(\mathbf{k}) | u_{\lambda'\mathbf{k}} \rangle, \quad (33)$$

where $\mathbf{p}(\mathbf{k}) = e^{-i\mathbf{k}\mathbf{r}} \mathbf{p} e^{i\mathbf{k}\mathbf{r}}$. Using $H_{1e}^0(\mathbf{k}) = e^{-i\mathbf{k}\mathbf{r}} H_{1e}^0 e^{i\mathbf{k}\mathbf{r}}$ and the relation: $[H_{1e}^0, \mathbf{r}] = -i \frac{\hbar}{m} \mathbf{p}$, we have

$$\mathbf{p}_{\lambda\lambda'}(\mathbf{k}) = \frac{m}{\hbar} \langle u_{\lambda\mathbf{k}} | \nabla_{\mathbf{k}} H_{1e}^0(\mathbf{k}) | u_{\lambda'\mathbf{k}} \rangle. \quad (34)$$

Eq. (34) enables us to numerically calculate the momentum matrix elements at discrete \mathbf{k} -points. Therefore, the light-matter interaction part of the second quantization Hamiltonian takes the following form:

$$\hat{H}^{e-L} = \frac{e}{m} \mathbf{A}(t) \cdot \sum_{\lambda\lambda'\mathbf{k}} \mathbf{p}_{\lambda\lambda'}(\mathbf{k}) c_{\lambda\mathbf{k}}^\dagger c_{\lambda'\mathbf{k}} + \frac{e^2 A^2}{2m} \sum_{\lambda\mathbf{k}} c_{\lambda\mathbf{k}}^\dagger c_{\lambda\mathbf{k}}. \quad (35)$$

The H^{e-e} derivation is presented in Appendix A. Thus, the many-body Hamiltonian in second quantization has the form:

$$\begin{aligned}
\hat{H} &= \hat{H}_{1e}^0 + \hat{H}^{e-e} + \hat{H}^{e-L} \\
&= \sum_{\lambda\mathbf{k}} \varepsilon_{\lambda\mathbf{k}} c_{\lambda\mathbf{k}}^\dagger c_{\lambda\mathbf{k}} \\
&\quad + \frac{1}{2} \sum_{\mathbf{k}, \mathbf{k}', \mathbf{q}} \sum_{\alpha\beta\gamma\delta} W_{\mathbf{k}, \mathbf{k}', \mathbf{q}}^{\alpha\beta\gamma\delta} c_{\alpha, \mathbf{k}+\mathbf{q}}^\dagger c_{\beta, \mathbf{k}'-\mathbf{q}}^\dagger c_{\gamma, \mathbf{k}} c_{\delta, \mathbf{k}'} \\
&\quad + \frac{e}{m} \mathbf{A}(t) \cdot \sum_{\lambda\lambda' \mathbf{k}} \mathbf{p}_{\lambda\lambda'}(\mathbf{k}) c_{\lambda\mathbf{k}}^\dagger c_{\lambda'\mathbf{k}} + \frac{e^2 \mathbf{A}^2}{2m} \sum_{\lambda\mathbf{k}} c_{\lambda\mathbf{k}}^\dagger c_{\lambda\mathbf{k}},
\end{aligned} \tag{36}$$

where the Coulomb interaction matrix elements are:

$$W_{\mathbf{k}, \mathbf{k}', \mathbf{q}}^{\alpha\beta\gamma\delta} = V_{e-e}(\mathbf{q}) \langle u_{\alpha\mathbf{k}+\mathbf{q}} | u_{\delta\mathbf{k}} \rangle \langle u_{\beta\mathbf{k}'-\mathbf{q}} | u_{\gamma\mathbf{k}'} \rangle, \tag{37}$$

with the 2-D Coulomb interaction in momentum space:

$$V_{e-e}(\mathbf{q}) = \frac{e^2}{2\varepsilon\varepsilon_0 L^2} \frac{1}{|\mathbf{q}|}. \tag{38}$$

2.4 Semiconductor Bloch Equations

With definition of density matrix elements,

$$\rho_{\lambda\lambda'}(\mathbf{k}) = \langle c_{\lambda'\mathbf{k}}^\dagger c_{\lambda\mathbf{k}} \rangle, \tag{39}$$

we use the equation of motion in Heisenberg picture for operator $c_{\lambda'\mathbf{k}}^\dagger c_{\lambda\mathbf{k}}$ and take its expectation value to have:

$$\frac{d}{dt} \langle c_{\lambda'\mathbf{k}}^\dagger c_{\lambda\mathbf{k}} \rangle = \frac{i}{\hbar} \langle [H, c_{\lambda'\mathbf{k}}^\dagger c_{\lambda\mathbf{k}}] \rangle. \tag{40}$$

Through the derivation in Appendix B, we have obtained the semiconductor Bloch equation(s) with Coulomb interaction in the Hartree-Fock approximation:

$$\begin{aligned}
\frac{d}{dt} \rho_{\lambda\lambda'}(\mathbf{k}) &= -\frac{i}{\hbar} (\varepsilon_\lambda(\mathbf{k}) - \varepsilon_{\lambda'}(\mathbf{k})) \rho_{\lambda\lambda'}(\mathbf{k}) - \frac{ie}{\hbar m} \mathbf{A}(t) \sum_{\mu} [\mathbf{p}_{\lambda\mu}(\mathbf{k}) \rho_{\mu\lambda'}(\mathbf{k}) - \rho_{\lambda\mu}(\mathbf{k}) \mathbf{p}_{\mu\lambda'}(\mathbf{k})] \\
&\quad + \frac{i}{\hbar} [\Omega_{\lambda\mu}(\mathbf{k}) \rho_{\mu\lambda'}(\mathbf{k}) - \rho_{\lambda\mu}(\mathbf{k}) \Omega_{\mu\lambda'}(\mathbf{k})] + \left. \frac{d}{dt} \rho_{\lambda\lambda'}(\mathbf{k}) \right|_{\text{scat.}},
\end{aligned} \tag{41}$$

where

$$\Omega_{\mu\nu}(\mathbf{k}) = \sum_{\alpha\beta\mathbf{q}} W_{\mathbf{k}, \mathbf{k}+\mathbf{q}, \mathbf{q}}^{\alpha\mu\beta\nu} \rho_{\alpha\beta}(\mathbf{k} + \mathbf{q}). \tag{42}$$

In Eq. (41), the last term is referred to as the scattering term, which characterizes the dephasing rates of interband polarization and collision rates and describes the relaxation of the electron and hole distributions. It is often approximated using the dephasing time parameter T_2 for interband polarization and two relaxation times called T_1' and T_1 for intraband

term ($\rho_{\lambda\lambda}(\mathbf{k})$). The scattering term corresponding to parameter T_1 indicates the combination between electrons in the conduction band and holes in the valence band can be neglected since the pulse duration time is too small (a few tens fs) compared with the combination (about a few to few tens ps)²⁶. The scattering term corresponding to the parameter T_1' describes the relaxation of electrons and holes into thermal distribution. The parameter T_1' usually being chosen satisfies $T_1' \gg T_2$ in numerical simulation of the linear absorption spectrum since we only focus on the linear transition between the valence and conduction bands, ignoring the relaxation into the thermal distribution. Therefore, in this work, we neglect this term for simplification. Here, we use

$$\left(\frac{d}{dt} \rho(\mathbf{k}) \Big|_{\text{scat.}} \right)_{\lambda\lambda'} \approx -\frac{\rho_{\lambda\lambda'}(\mathbf{k})}{T_2} \quad \forall \lambda \neq \lambda'. \quad (43)$$

This approximation disregards nonlinear and non-Markovian effects²⁷, which are not considered in this particular study. Including Eq. (43) into Eq. (41), we obtain the semiconductor Bloch equations²⁷:

$$\begin{aligned} \frac{d}{dt} \rho_{\lambda\lambda'}(\mathbf{k}) = & -\frac{i}{\hbar} (\varepsilon_{\lambda}(\mathbf{k}) - \varepsilon_{\lambda'}(\mathbf{k})) \rho_{\lambda\lambda'}(\mathbf{k}) - \frac{ie}{\hbar m} \mathbf{A}(t) \sum_{\mu} (\mathbf{p}_{\lambda\mu}(\mathbf{k}) \rho_{\mu\lambda'}(\mathbf{k}) - \rho_{\lambda\mu}(\mathbf{k}) \mathbf{p}_{\mu\lambda'}(\mathbf{k})) \\ & + \frac{i}{\hbar} (\Omega_{\lambda\mu}(\mathbf{k}) \rho_{\mu\lambda'}(\mathbf{k}) - \rho_{\lambda\mu}(\mathbf{k}) \Omega_{\mu\lambda'}(\mathbf{k})) - \frac{1}{T_2} \rho_{\lambda\lambda'}(\mathbf{k}) \quad \forall \lambda \neq \lambda', \end{aligned} \quad (44)$$

and,

$$\begin{aligned} \frac{d}{dt} \rho_{\lambda\lambda}(\mathbf{k}) = & -\frac{ie}{\hbar m} \mathbf{A}(t) \sum_{\mu} (\mathbf{p}_{\lambda\mu}(\mathbf{k}) \rho_{\mu\lambda}(\mathbf{k}) - \rho_{\lambda\mu}(\mathbf{k}) \mathbf{p}_{\mu\lambda}(\mathbf{k})) \\ & + \frac{i}{\hbar} (\Omega_{\lambda\mu}(\mathbf{k}) \rho_{\mu\lambda}(\mathbf{k}) - \rho_{\lambda\mu}(\mathbf{k}) \Omega_{\mu\lambda}(\mathbf{k})), \end{aligned} \quad (45)$$

where,

$$\Omega_{\mu\nu}(\mathbf{k}) = \sum_{\alpha\beta\mathbf{q}} W_{\mathbf{k},\mathbf{k}+\mathbf{q},\mathbf{q}}^{\alpha\mu\beta\nu} \rho_{\alpha\beta}(\mathbf{k} + \mathbf{q}). \quad (46)$$

2.5 Polarization Density

Polarization density is calculated from the trace of the product of the dipole matrix and density matrix

$$\mathbf{P}(t) = \frac{e}{L^2} \sum_{\mathbf{k}} \text{Tr} [\vec{\xi}(\mathbf{k}) \rho(\mathbf{k}, t)] = \frac{e}{L^2} \sum_{\lambda\lambda'} \vec{\xi}_{\lambda\lambda'}(\mathbf{k}) \rho_{\lambda'\lambda}(\mathbf{k}, t). \quad (47)$$

The sum over all \mathbf{k} -points in the first BZ is approximately given by the integral

$$\sum_{\mathbf{k}} \dots \rightarrow \frac{L^2}{(2\pi)^2} \int_{\text{BZ}} d^2k \dots \quad (48)$$

Including it into polarization density Eq. (47), we have:

$$\mathbf{P}(t) = \frac{e}{L^2} \sum_{\mathbf{k}} \text{Tr} [\vec{\xi}(\mathbf{k}) \rho(\mathbf{k}, t)] = \frac{1}{(2\pi)^2} \sum_{\lambda\lambda'} \int \vec{\xi}_{\lambda\lambda'}(\mathbf{k}) \rho_{\lambda'\lambda}(\mathbf{k}, t) d\mathbf{k}, \quad (49)$$

in which the dipole $\vec{\xi}_{\lambda\lambda'}(\mathbf{k})$ can be calculated through $\mathbf{p}_{\lambda\lambda'}(\mathbf{k})$ (derived in appendix C):

$$\vec{\xi}_{\lambda\lambda'}(\mathbf{k}) = -\frac{i\hbar}{m} \frac{\mathbf{p}_{\lambda\lambda'}(\mathbf{k})}{\varepsilon_{\lambda}(\mathbf{k}) - \varepsilon_{\lambda'}(\mathbf{k})}. \quad (50)$$

The numerical result of Eq. (49) will be obtained by using the Riemann sum integral.

3 Numerical Methods

3.1 Numerical Evaluation of The Sum over \mathbf{k}

Monolayer TMD's actual lattice, denoted as MX_2 , possesses the D_{3h} point-group symmetry, which is illustrated in Fig. 1. The 2D first Brillouin zone takes on the shape of a hexagon. This study concentrates on the linear abortion spectrum, a feature that relies heavily on the \mathbf{k} -point with the direct band gap of this material. To numerical calculate the Eq. (49), we need to take the numerical integral over the first BZ, which is inconvenient when working with the hexagon shape. Furthermore, a direct band gap is observed at the K and K' points in the first BZ, as depicted in Fig. (2). There are three K and three K' points situated at the edge of the first BZ as shown in Fig. 3, with each point being shared between three BZ. Consequently, we need to calculate the average numerical position by adding up the positions and then dividing by the number of points, which can pose further challenges for the many-body problems we are addressing.

To address this, we introduce the use of the rhombus primitive cell, as shown in Fig. 3. This cell is constructed from 4 M-points located between K and K' on the edge of the hexagon, enabling us to focus on the properties of K and K' points both individually and in pairs.

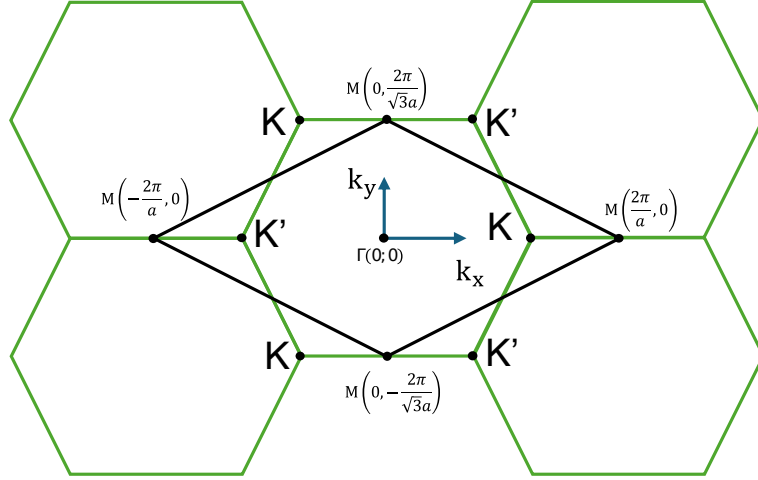


Figure 3: Rhombus primitive unit cell constructed through four M-points, which has the same area as the first Brillouin zone (the green Hexagon with six corners at "K-point" and "K'-point")

To establish a new coordinate system, we will utilize the two unit vectors located at the left corner of the rhombus $u_1 = (2\pi/3a, 2\pi/\sqrt{3}a)$ and $u_2 = (2\pi/3a, -2\pi/\sqrt{3}a)$ as shown in Fig. 4, which will be reference to as the "Rhombus basis" hereinafter. Consider a point \mathbf{P} , which have coordinate (v_1, v_2) in rhombus basis and coordinate (k_x, k_y) in rectangular basis. These

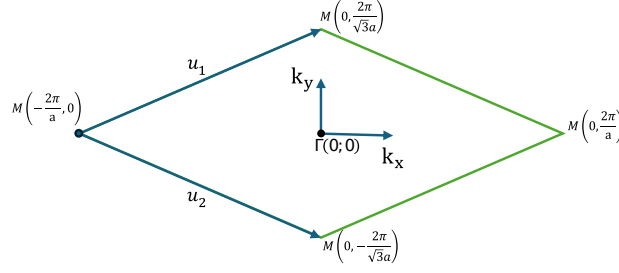


Figure 4: New basis Based on the rhombus unit vectors

coordinates have a relation through the transformation:

$$\begin{pmatrix} k_x \\ k_y \end{pmatrix} = \frac{2\pi}{a} \begin{pmatrix} 1 & 1 \\ \frac{1}{\sqrt{3}} & -\frac{1}{\sqrt{3}} \end{pmatrix} \begin{pmatrix} v_1 \\ v_2 \end{pmatrix} - \begin{pmatrix} \frac{2\pi}{a} \\ 0 \end{pmatrix}, \quad \begin{pmatrix} v_1 \\ v_2 \end{pmatrix} = \frac{a}{4\pi} \begin{pmatrix} 1 & \sqrt{3} \\ 1 & -\sqrt{3} \end{pmatrix} \begin{pmatrix} k_x \\ k_y \end{pmatrix} + \begin{pmatrix} 1/2 \\ 1/2 \end{pmatrix}, \quad (51)$$

Since the v_1, v_2 is a continuous variable, we need to convert it into discrete coordinates to proceed with a numerical solution. To do this, we divide the vectors u_1 and u_2 into n equal segments, which are then labeled as n_1 and n_2 , respectively. We discrete the continuous coordinate (v_1, v_2) in term of (n_1, n_2) :

$$\begin{cases} v_1 = n_1 \frac{u_1}{n} \\ v_2 = n_2 \frac{u_2}{n} \end{cases}, n_1, n_2 \in \{0, 1, \dots, n\}.$$

3.2 Cut-off K-point Technique

In our research, we are focusing on the transition between the valence and conduction bands around the K and K' points. We achieve this by using a small-intensity electric field and limiting the photon energy to around the band gap energy E_{gap} . However, the calculation of the Coulomb interaction for every point in the rhombus with other points all over the rhombus is not efficient in terms of time cost, and convergence. As demonstrated in the 2-D Coulomb interaction Eq. (38), the Coulomb potential is inversely proportional to the distance between two points in k-space. To address this issue, we are introducing a technique to limit the points taken into account in the Coulomb interaction part.

In the diagram shown in Fig. 5, a circle is drawn around the K' point with a radius of k_{cut} . When calculating the Eq. (44) at a k-point, if this k-point is outside the circle, we use

$$\Omega_{\mu\nu}(\mathbf{k}) = 0 \quad \forall \mu, \nu.$$

When dealing with a k-point inside the circle, we only consider interactions with other points inside the circle. This reduces the computational load significantly. In a 2-dimensional system, each doubling of k-points results in a 32-fold increase in simulation time (we calculate

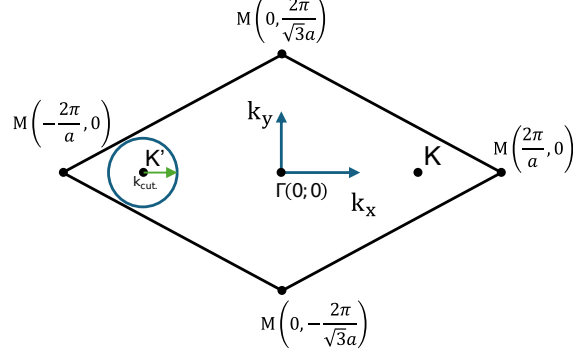


Figure 5: k-radius show the cutoff circle around K' points

on both K and K'). However, by focusing on the K/K' point and reducing the number of k -points, the time cost only increases by approximately 8 to 10 times.

In summary, we approximate the Coulomb interaction matrix elements:

$$W_{\mathbf{k}, \mathbf{k}', \mathbf{q}}^{\alpha\mu\beta\nu} \approx W_{\mathbf{k}, \mathbf{k}', \mathbf{q}}^{\alpha\mu\beta\nu} \theta(k_{cut} - |\mathbf{k} - \mathbf{k}_{K'}|) \theta(k_{cut} - |\mathbf{k}' - \mathbf{k}_{K'}|).$$

Where $\theta(k)$ represents the Heaviside function, the Coulomb interaction is excluded if either point is outside the circle. The same process applies to the K point.

3.3 Absorption Coefficient

The linear absorption spectrum is determined by²⁷

$$\alpha(\omega) \propto \text{Im} \left\{ \frac{P(\omega)}{E(\omega)} \right\}. \quad (52)$$

In which $\mathbf{P}(\omega) = \int_{-\infty}^{\infty} \mathbf{P}(t) e^{i\omega t} dt$ and $\mathbf{E}(\omega) = \int_{-\infty}^{\infty} \mathbf{E}(t) e^{i\omega t} dt$ are the Fourier transforms for polarization density and electric field. These integrals can be approximated using a Riemann sum with the cut-off point by using conditions $\mathbf{E}(t_{cutoff}) \lesssim 10^{-6} |\max \mathbf{E}(t)|$ and $\mathbf{P}(t_{cutoff}) \lesssim 10^{-6} |\max \mathbf{P}(t)|$. In this work, we are using the electric field in the form:

$$\mathbf{E}(t) = E_0 e^{-\frac{t^2}{\tau_L^2}} (\cos(\omega_0 t), 0), \quad (53)$$

with the E_0 is the maximal amplitude, $\hbar\omega_0 = E_{\text{gap}}$, τ_L is the duration of the Gaussian envelope, and t is time, all will be calculated in SI units. The electric field and its Fourier transform shape are shown in Fig. 6.

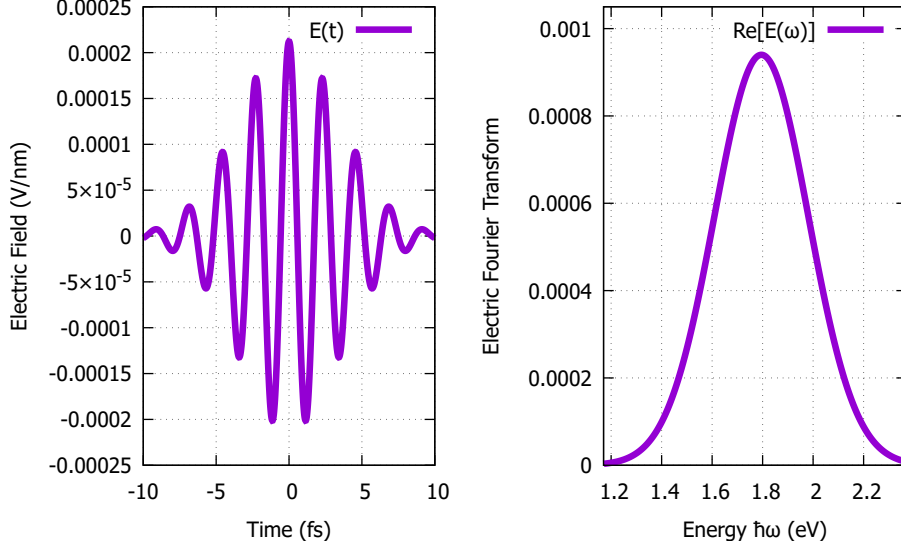


Figure 6: Electric field on Ox direction and its Fourier Transform

4 Results and Discussion

In the previous study¹², the absorption spectrum of MoS₂ at $T = 5K$ was measured and presented in Fig. 7. The results revealed two exciton resonances labeled A and B, which were observed at energy levels of 1.9 and 2.1 eV, respectively. Additionally, a small trion peak was observed before the A peak. The splitting between the exciton and trion absorption peaks was approximately 34 meV at 5K.

When solving the SBE numerically, we use the following parameters: $E_0 = \frac{3}{\sqrt{2}} \times 10^3$ V/cm, $\hbar\omega_0 = E_{\text{gap}} = 1.77$ eV, time step $\Delta t = 0.02$ fs, $T_2 = 20$ fs, and the cutoff radius of 3 nm^{-1} around the K (K') point for the Coulomb interaction. Since we focus on the linear absorption spectrum to calculate the exciton binding, we must limit the numerical error around ω_0 point. Therefore, we need to choose the τ_L as small as possible to flatten the peak of the Fourier transform of the Electric field. But as we decrease the τ_L , the time for the electric field to pass through the material becomes so fast that we have to decrease the time step to catch up with the system's response to the external field. Therefore, we choose the $\tau_L = 5 \text{ fs}$ in correspond with time step Δt . By simulating with the given parameters, the excited carrier density is small ($\sim 10^7 \text{ cm}^{-2}$) so nonlinear effects can be ignored. We perform Fourier transforms to the frequency domain corresponding to the energy domain from $E_g - 1 \text{ eV}$ to $E_g + 1 \text{ eV}$. There are main parameters we can adjust to obtain results that agree with recent measurements or predict future measurements: relative permittivity ε , dephasing time T_2 .

In Fig. 8, our results for calculating the absorption spectrum with LDA parameters are presented, where the relative permittivity is $\varepsilon = 2.5$ with difference T_2 . As T_2 increases, two main peaks become clearer at 1.528 and 1.640 eV, indicating a binding energy of $E_{\text{bind.}} = E_{\text{gap}} - 1.528 \text{ eV} = 0.242 \text{ eV}$.

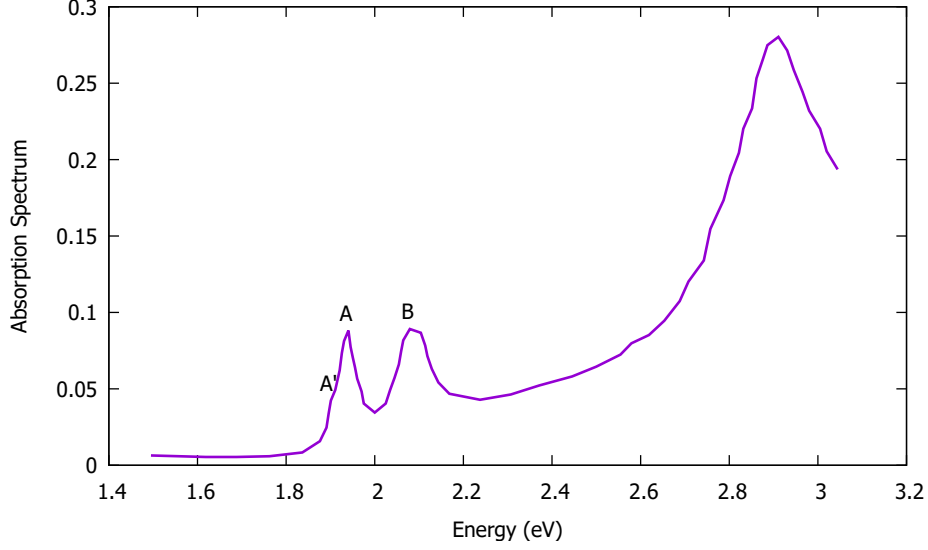


Figure 7: Absorption spectrum of MoS₂ at $T = 5K$ extracted from¹², two exciton resonances labeled by A and B, and small trion peak labeled with A'.

We present our results for calculating the absorption spectrum using the LDA parameter and the difference dielectric ε in Fig. 9. As ε increases, two main peaks shift to the right, which indicates that exciton energy decreases. The exciton binding energy for several values of ε is shown in Tab. 2.

In Fig. 10, we present our numerical results with varying numbers of k-grid points, using a

ε	1.0	1.5	2.0	2.5
$E_{\text{bind.}}(eV)$	0.95	0.55	0.36	0.24

Table 2: Exciton binding energy with difference ε

dielectric constant of $\varepsilon = 2.5$ to demonstrate the convergence of the results. The calculations show that to obtain the convergent result, a fairly large number of k points are required. To strike a balance between precision and computational time cost, we opt for $nk = 60$ for the subsequent calculations.

With a small T_2 of 15 fs, the results in Fig. 8 have already shown two main exciton peaks in comparison with the experimental results in Fig. 7. However, as the T_2 increases, we can see smaller exciton peaks in the absorption spectrum, as described in Fig. 8. These A and B exciton resonances involve the conduction bands and two valence bands (split due to SOC) near the K and K' points, as shown in the band structure in Fig. 2. The erasing of two peaks under small T_2 can be attributed to the strong scattering. In our results shown in Fig. 8 and the experiment by Zhang et al.¹² in Fig. 7, our result is smaller than some previous calculations predicting the binding energy between 0.5 eV to 1 eV¹³⁻¹⁶. This result agrees

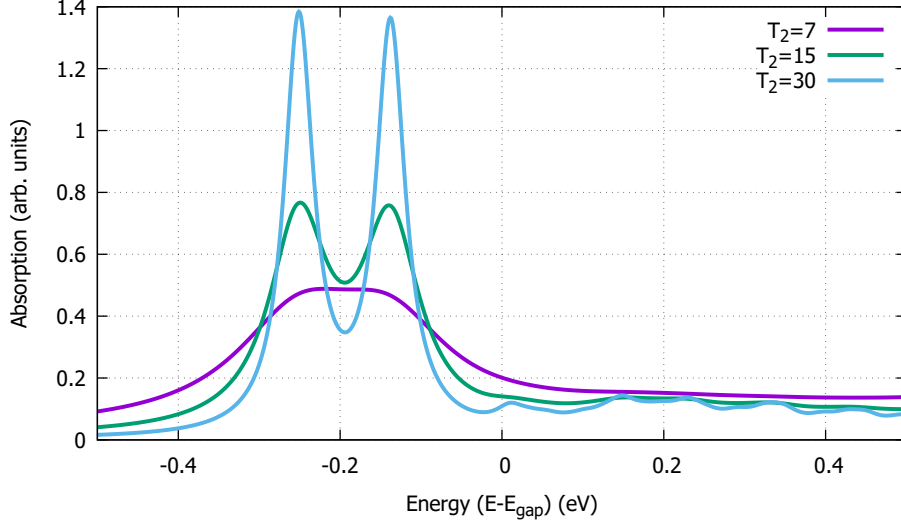


Figure 8: Absorption spectrum with difference T_2

with more precise calculations and measurements^{11;12;17;28}. The difference in band gap energy can be attributed to the use of ab initio calculations in our model²⁰. This model does not consider the band gap shift caused by the underlying layers and temperature variations in the experimental measurement. The absence of the trion peak in Fig. 8 in comparison with Fig. 7 is due to the trion involving interaction between three particles (2 holes and 1 electron for a positive trion, 1 hole, and 2 electrons for a negative trion), which is not included in the Hartree-Fock approximation. To observe the trion peak, it is suggested to go beyond the Hartree-Fock Approximation in established equations.

This model is effective and has advantages for calculation over BZ, but it also has disadvantages and requires denser k-grids for results to converge (as shown in Fig. 10) compared to ab initio calculations or effective mass approximation models. The bare Coulomb interaction works well in calculating the linear absorption spectrum, but for a more realistic case, the screening effect of the Coulomb interaction must be taken into account^{29;30}, especially when we want to go beyond the weak excitation limit. It's worth noting that the scattering term in form of Eq. (43) is proved to be a good approximation without requiring further techniques in showing two main exciton peaks and predicting other smaller peaks. However, for a more realistic representation, the scattering term in Eq. (44) can also be expanded in terms of electron-electron and electron-phonon scattering terms, which would provide a more comprehensive analysis of the system under consideration. Additionally, it is crucial to consider the implications of these findings in the context of practical applications and the broader theoretical framework.

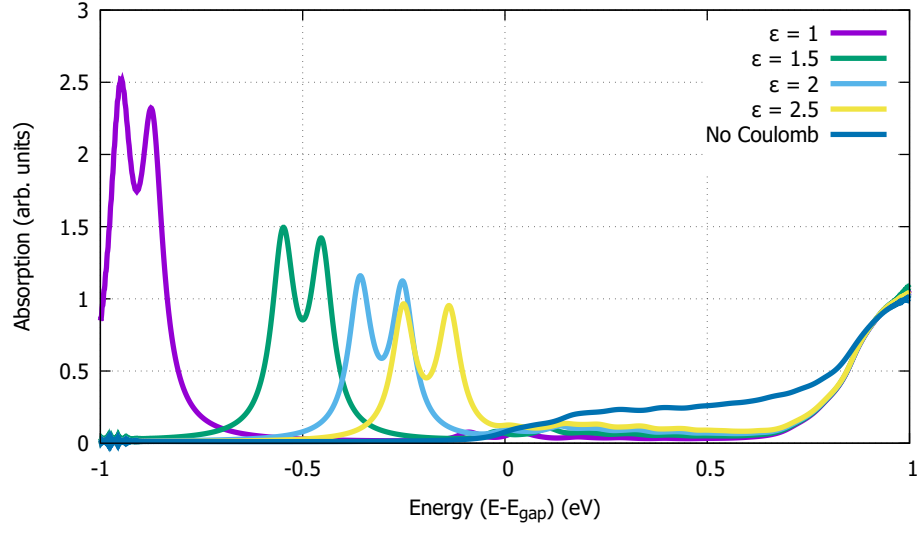


Figure 9: Absorption spectrum with difference dielectric ε and without Coulomb interaction

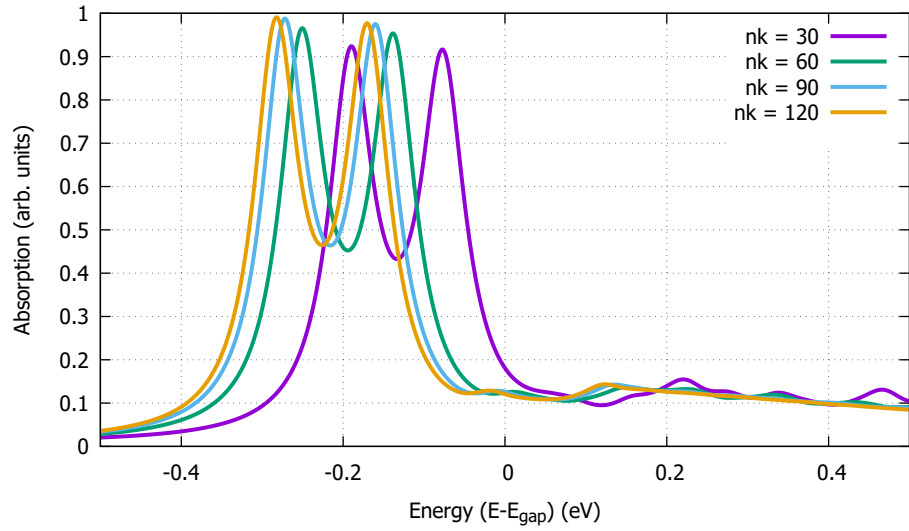


Figure 10: Absorption spectrum with difference number of k-points

5 Conclusion and Further Research

In our research, we have calculated the linear absorption of monolayer MoS₂ using a tight-binding three-band model with spin-orbit coupling through semiconductor Bloch equations in Hartree-Fock approximation. We have varied three parameters to analyze their relation with the absorption spectrum and found that the results align with other calculations, indicating a significant binding energy up to two magnitude in comparison with other bulk semiconductors.

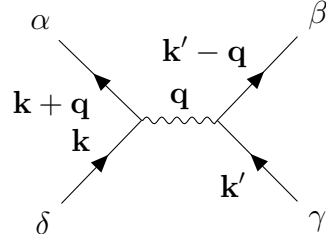
We have encountered some limitations, like the time-consuming process of enhancing the k-grid for better convergence and the discrepancy in the bandgap position as compared to experimental data. We also have observed that the bare Coulomb interaction might not be adequate for an accurate depiction and should be fine-tuned for better outcomes.

For further researches, we can utilize this three-band tight-binding model to calculate other optoelectronic phenomena affected by excitons, such as high harmonic generation (HHG), high-order sideband generation (HSG), and photovoltaic current. When calculating the photovoltaic effect, it's important to consider the influence of Coulomb interactions. Without the consideration of Coulomb interactions, only the shift current is apparent, as we've calculated the current tensors as per Ref.³¹. However, once we include the Coulomb interaction, the ballistic current becomes significant, and the shift tensor current is also affected. It's crucial to account for Coulomb interactions to obtain a realistic picture of the photovoltaic effect.

Appendices

A Coulomb matrix elements

The Coulomb matrix elements is



$$\begin{aligned}
 W_{\mathbf{k}, \mathbf{k}', \mathbf{q}}^{\alpha\beta\gamma\delta} &= \langle \psi_{\alpha\mathbf{k} + \mathbf{q}} \psi_{\beta\mathbf{k}' - \mathbf{q}} | V_{e-e} | \psi_{\gamma\mathbf{k}'} \psi_{\delta\mathbf{k}} \rangle = \\
 &= \int \frac{d^3r}{V} \int \frac{d^3r'}{V} e^{-i\mathbf{q}(\mathbf{r} - \mathbf{r}')} u_{\alpha\mathbf{k} + \mathbf{q}}^*(\mathbf{r}) u_{\beta\mathbf{k}' - \mathbf{q}}^*(\mathbf{r}') V_{e-e}(\mathbf{r} - \mathbf{r}') u_{\gamma\mathbf{k}'}(\mathbf{r}') u_{\delta\mathbf{k}}(\mathbf{r}), \quad (54)
 \end{aligned}$$

with

$$V_{e-e}(\mathbf{r}) = \frac{e^2}{4\pi\epsilon\epsilon_0} \frac{1}{|\mathbf{r}|}, \quad (55)$$

we expand it using Fourier transform

$$\begin{aligned}
 V_{e-e}(\mathbf{q}) &= \int \frac{d^3\mathbf{r}}{V} V_{e-e}(\mathbf{r}) e^{-i\mathbf{q}\cdot\mathbf{r}} = \frac{e^2}{4\pi\epsilon\epsilon_0 V} \int d^3\mathbf{r} \frac{1}{|\mathbf{r}|} e^{-i\mathbf{q}\cdot\mathbf{r}} \\
 &= \frac{e^2}{4\pi\epsilon\epsilon_0 V} \int_0^\infty \int_0^{2\pi} \int_{-\pi}^\pi \frac{1}{r} r^2 e^{-iqr \cos(\theta)} dr d\varphi \cos(\theta) d\theta \\
 &= \frac{e^2}{2\epsilon\epsilon_0 V} \int_0^\infty \int_{-1}^1 r dr d\cos\theta e^{iqr \cos\theta} = -\frac{i}{q} \frac{e^2}{2\epsilon\epsilon_0 V} \int_0^\infty dr (e^{iqr} - e^{-iqr}) \\
 &= -\frac{i}{q} \frac{e^2}{2\epsilon\epsilon_0 V} \lim_{\gamma \rightarrow 0} \int_0^\infty dr (e^{iqr} - e^{-iqr}) e^{-\gamma r} \\
 &= \frac{e^2}{2\epsilon\epsilon_0 V} \lim_{\gamma \rightarrow 0} \left(\int_0^\infty \frac{e^{(iq-\gamma)r}}{iq-\gamma} dr - \int_0^\infty \frac{e^{-(iq+\gamma)r}}{iq+\gamma} dr \right) = \frac{e^2}{\epsilon\epsilon_0 V} \frac{1}{q^2}. \quad (56)
 \end{aligned}$$

Including Eq. (56) into Eq. (54), and do reverse Fourier transform

$$\begin{aligned}
 V_{e-e}(\mathbf{r}) &= \sum_{\mathbf{q}} V_{e-e}(\mathbf{q}) e^{i\mathbf{q}\cdot\mathbf{r}} = \sum_{\mathbf{q}_{||}, \mathbf{q}_{\perp}} \frac{e^2}{\epsilon\epsilon_0 V} \frac{1}{\mathbf{q}_{||}^2 + q_{\perp}^2} e^{i\mathbf{q}_{||}\mathbf{r}_{||}} e^{iq_{\perp}r_{\perp}} \\
 &= \sum_{\mathbf{q}_{||}} \frac{1}{2\pi/L_z} \frac{e^2}{\epsilon\epsilon_0 V} e^{i\mathbf{q}_{||}\mathbf{r}_{||}} \int dq_{\perp} \frac{e^{iq_{\perp}r_{\perp}}}{\mathbf{q}_{||}^2 + q_{\perp}^2}, \quad (57)
 \end{aligned}$$

$$\begin{aligned}
 \bullet \int_{-\infty}^{\infty} dx \frac{e^{iax}}{a^2 + x^2} &= \oint dz \frac{e^{iaz}}{(z+ia)(z-ia)} = 2\pi i \text{Res}_{z=ia} \left[\frac{e^{iaz}}{(z+ia)(z-ia)} \right] \\
 &= 2\pi i \lim_{z \rightarrow ia} \frac{e^{iaz}}{(z+ia)(z-ia)} (z-ia) = 2\pi i \frac{e^{-ax}}{2ia} = \frac{\pi e^{-ax}}{a} \quad (a > 0) \quad (58)
 \end{aligned}$$

$$\Rightarrow (57) = \sum_{\mathbf{q}_{||}} \frac{e^2}{2\epsilon\epsilon_0 L^2} e^{i\mathbf{q}_{||}\mathbf{r}_{||}} \frac{e^{-|\mathbf{q}_{||}||\mathbf{r}_{\perp}|}}{|\mathbf{q}_{||}|} = \sum_{\mathbf{q}_{||}} V_{||}^{2D}(\mathbf{q}_{||}, \mathbf{r}_{\perp}) e^{i\mathbf{q}_{||}\mathbf{r}_{||}} \quad (59)$$

$$\therefore V_{||}^{2D}(\mathbf{q}_{||}, z) = \frac{e^2}{2\varepsilon\varepsilon_0 L^2} \frac{e^{-|\mathbf{q}_{||}|z}}{|\mathbf{q}_{||}|}. \quad (60)$$

Include Eq. (60) back into Eq. (54) through Eq. (59) for 2D-case

$$\begin{aligned} W_{\mathbf{k}, \mathbf{k}', \mathbf{q}}^{\alpha\beta\gamma\delta} &= \int \int d\mathbf{r}_1 d\mathbf{r}_2 u_{\mathbf{k}_{||}+\mathbf{q}_{||}}^{\alpha\dagger}(\mathbf{r}_1) u_{\mathbf{k}'_{||}-\mathbf{q}_{||}}^{\beta\dagger}(\mathbf{r}_2) V^{3D}(\mathbf{r}_2 - \mathbf{r}_1) e^{i\mathbf{q}_{||}(\mathbf{r}_2-\mathbf{r}_1)} u_{\mathbf{k}'_{||}}^{\gamma}(\mathbf{r}_2) u_{\mathbf{k}_{||}}^{\delta}(\mathbf{r}_1) \\ &= \frac{e^2}{2\varepsilon\varepsilon_0 L^2} \sum_{\mathbf{q}'_{||}} \int \int d\mathbf{r}_1 d\mathbf{r}_2 u_{\mathbf{k}_{||}+\mathbf{q}_{||}}^{\alpha\dagger}(\mathbf{r}_1) u_{\mathbf{k}'_{||}-\mathbf{q}_{||}}^{\beta\dagger}(\mathbf{r}_2) e^{i\mathbf{q}'_{||}(\mathbf{r}_2-\mathbf{r}_1)} \frac{e^{-|\mathbf{q}'_{||}|z_2-z_1}}{|\mathbf{q}'_{||}|} e^{i\mathbf{q}_{||}(\mathbf{r}_2-\mathbf{r}_1)} u_{\mathbf{k}'_{||}}^{\gamma}(\mathbf{r}_2) u_{\mathbf{k}_{||}}^{\delta}(\mathbf{r}_1), \end{aligned} \quad (61)$$

We apply long-wave approximation for the sum over $\mathbf{q}'_{||}$, take the limit $z_1, z_2 \rightarrow 0$. Therefore the $W_{\mathbf{k}, \mathbf{k}', \mathbf{q}}^{\alpha\beta\gamma\delta}$ take the form:

$$W_{\mathbf{k}, \mathbf{k}', \mathbf{q}}^{\alpha\beta\gamma\delta} = \frac{e^2}{2\varepsilon\varepsilon_0 L^2} \frac{1}{|\mathbf{q}|} \langle u_{\mathbf{k}+\mathbf{q}}^{\alpha} | u_{\mathbf{k}}^{\delta} \rangle \langle u_{\mathbf{k}'-\mathbf{q}}^{\beta} | u_{\mathbf{k}'}^{\gamma} \rangle \quad (62)$$

B Equation of Motion

We consider Hamiltonian (36), using Heisenberg equation of motion part by part with creation and annihilation operator satisfies relation (28):

$$\begin{aligned}
[H_{1e}^0, c_{\alpha\mathbf{k}}^\dagger c_{\beta\mathbf{k}}] &= \sum_{\mathbf{k}'\lambda} \varepsilon_{\lambda,\mathbf{k}'} [c_{\lambda\mathbf{k}'}^\dagger c_{\lambda\mathbf{k}'}, c_{\alpha\mathbf{k}}^\dagger c_{\beta\mathbf{k}}] \\
&= \sum_{\mathbf{k}'\lambda} \varepsilon_{\lambda,\mathbf{k}'} (c_{\lambda\mathbf{k}'}^\dagger c_{\lambda\mathbf{k}'} c_{\alpha\mathbf{k}}^\dagger c_{\beta\mathbf{k}} - c_{\alpha\mathbf{k}}^\dagger c_{\beta\mathbf{k}} c_{\lambda\mathbf{k}'}^\dagger c_{\lambda\mathbf{k}'}) \\
&= \sum_{\mathbf{k}\lambda'} \varepsilon_{\lambda,\mathbf{k}} (c_{\lambda\mathbf{k}}^\dagger \delta_{\lambda\alpha} \delta_{\mathbf{k}\mathbf{k}'} c_{\beta\mathbf{k}} - c_{\lambda\mathbf{k}}^\dagger c_{\alpha\mathbf{k}}^\dagger c_{\lambda\mathbf{k}'} c_{\beta\mathbf{k}} - c_{\alpha\mathbf{k}}^\dagger \delta_{\beta\lambda} \delta_{\mathbf{k}\mathbf{k}'} c_{\lambda\mathbf{k}'} + c_{\alpha\mathbf{k}}^\dagger c_{\lambda\mathbf{k}'}^\dagger c_{\beta\mathbf{k}} c_{\lambda\mathbf{k}'}) \\
&= \sum_{\mathbf{k}\lambda'} \varepsilon_{\lambda,\mathbf{k}} (c_{\lambda\mathbf{k}}^\dagger \delta_{\lambda\alpha} \delta_{\mathbf{k}\mathbf{k}'} c_{\beta\mathbf{k}} - \cancel{c_{\alpha\mathbf{k}}^\dagger c_{\lambda\mathbf{k}'}^\dagger c_{\beta\mathbf{k}} c_{\lambda\mathbf{k}'}} - c_{\alpha\mathbf{k}}^\dagger \delta_{\beta\lambda} \delta_{\mathbf{k}\mathbf{k}'} c_{\lambda\mathbf{k}'} + \cancel{c_{\alpha\mathbf{k}}^\dagger c_{\lambda\mathbf{k}'}^\dagger c_{\beta\mathbf{k}} c_{\lambda\mathbf{k}'}}) \\
&= (\varepsilon_\alpha(\mathbf{k}) - \varepsilon_\beta(\mathbf{k})) c_{\alpha\mathbf{k}}^\dagger c_{\beta\mathbf{k}}
\end{aligned} \tag{63}$$

$$\begin{aligned}
[H^{e-L}, c_{\alpha\mathbf{k}}^\dagger c_{\beta\mathbf{k}}] &= \sum_{\lambda\lambda'\mathbf{k}'} \mathbf{p}_{\lambda\lambda'}(\mathbf{k}') [c_{\lambda\mathbf{k}'}^\dagger c_{\lambda'\mathbf{k}'}, c_{\alpha\mathbf{k}}^\dagger c_{\beta\mathbf{k}}] + \sum_{\lambda\mathbf{k}'} \frac{e^2 A^2}{2m} [\cancel{c_{\lambda\mathbf{k}'}^\dagger c_{\lambda\mathbf{k}'}, c_{\alpha\mathbf{k}}^\dagger c_{\beta\mathbf{k}}}] \\
&= \sum_{\lambda\lambda'\mathbf{k}'} \mathbf{p}_{\lambda\lambda'}(\mathbf{k}') (c_{\lambda\mathbf{k}'}^\dagger c_{\lambda'\mathbf{k}'} c_{\alpha\mathbf{k}}^\dagger c_{\beta\mathbf{k}} - c_{\alpha\mathbf{k}}^\dagger c_{\beta\mathbf{k}} c_{\lambda\mathbf{k}'}^\dagger c_{\lambda'\mathbf{k}'}) \\
&= \sum_{\lambda\lambda'\mathbf{k}'} \mathbf{p}_{\lambda\lambda'}(\mathbf{k}') (c_{\lambda\mathbf{k}'}^\dagger \delta_{\lambda'\alpha} \delta_{\mathbf{k}\mathbf{k}'} c_{\beta\mathbf{k}} - c_{\lambda\mathbf{k}'}^\dagger c_{\alpha\mathbf{k}}^\dagger c_{\lambda'\mathbf{k}'} c_{\beta\mathbf{k}} - c_{\alpha\mathbf{k}}^\dagger \delta_{\beta\lambda} \delta_{\mathbf{k}\mathbf{k}'} c_{\lambda'\mathbf{k}'} + c_{\alpha\mathbf{k}}^\dagger c_{\lambda\mathbf{k}'}^\dagger c_{\beta\mathbf{k}} c_{\lambda'\mathbf{k}'}) \\
&= \sum_{\lambda\lambda'\mathbf{k}'} \mathbf{p}_{\lambda\lambda'}(\mathbf{k}') (c_{\lambda\mathbf{k}'}^\dagger \delta_{\lambda'\alpha} \delta_{\mathbf{k}\mathbf{k}'} c_{\beta\mathbf{k}} - \cancel{c_{\lambda\mathbf{k}'}^\dagger c_{\alpha\mathbf{k}}^\dagger c_{\lambda'\mathbf{k}'} c_{\beta\mathbf{k}}} - c_{\alpha\mathbf{k}}^\dagger \delta_{\beta\lambda} \delta_{\mathbf{k}\mathbf{k}'} c_{\lambda'\mathbf{k}'} + \cancel{c_{\alpha\mathbf{k}}^\dagger c_{\lambda\mathbf{k}'}^\dagger c_{\beta\mathbf{k}} c_{\lambda'\mathbf{k}'}}) \\
&= \sum_{\lambda} (\mathbf{p}_{\lambda\alpha}(\mathbf{k}) c_{\lambda\mathbf{k}}^\dagger c_{\beta\mathbf{k}} - \mathbf{p}_{\beta\lambda}(\mathbf{k}) c_{\alpha\mathbf{k}}^\dagger c_{\lambda\mathbf{k}})
\end{aligned} \tag{64}$$

$$\begin{aligned}
[H^{Coulomb}, c_{\lambda\mathbf{k}''}^\dagger c_{\lambda'\mathbf{k}''}] &= \sum_{\mathbf{k},\mathbf{k}',\mathbf{q}} \sum_{\alpha\beta\gamma\delta} W_{\mathbf{k},\mathbf{k}',\mathbf{q}}^{\alpha\beta\gamma\delta} [c_{\alpha,\mathbf{k}+\mathbf{q}}^\dagger c_{\beta,\mathbf{k}'-\mathbf{q}}^\dagger c_{\gamma,\mathbf{k}\delta,\mathbf{k}'} c_{\lambda\mathbf{k}''}^\dagger c_{\lambda'\mathbf{k}''}] \\
&= \sum_{\mathbf{k},\mathbf{k}',\mathbf{q}} \sum_{\alpha\beta\gamma\delta} W_{\mathbf{k},\mathbf{k}',\mathbf{q}}^{\alpha\beta\gamma\delta} (c_{\alpha,\mathbf{k}+\mathbf{q}}^\dagger c_{\beta,\mathbf{k}'-\mathbf{q}}^\dagger c_{\gamma,\mathbf{k}\delta,\mathbf{k}'} c_{\lambda\mathbf{k}''}^\dagger c_{\lambda'\mathbf{k}''} - c_{\lambda\mathbf{k}''}^\dagger c_{\lambda'\mathbf{k}''} c_{\alpha,\mathbf{k}+\mathbf{q}}^\dagger c_{\beta,\mathbf{k}'-\mathbf{q}}^\dagger c_{\gamma,\mathbf{k}\delta,\mathbf{k}'}) \\
&\bullet \quad c_{\alpha,\mathbf{k}+\mathbf{q}}^\dagger c_{\beta,\mathbf{k}'-\mathbf{q}}^\dagger c_{\gamma,\mathbf{k}\delta,\mathbf{k}'} c_{\lambda\mathbf{k}''}^\dagger c_{\lambda'\mathbf{k}''} = c_{\alpha,\mathbf{k}+\mathbf{q}}^\dagger c_{\beta,\mathbf{k}'-\mathbf{q}}^\dagger c_{\gamma,\mathbf{k}} \delta_{\lambda,\delta} \delta_{\mathbf{k}',\mathbf{k}''} c_{\lambda'\mathbf{k}''} - c_{\alpha,\mathbf{k}+\mathbf{q}}^\dagger c_{\beta,\mathbf{k}'-\mathbf{q}}^\dagger c_{\gamma,\mathbf{k}} c_{\lambda\mathbf{k}''}^\dagger c_{\delta,\mathbf{k}'} c_{\lambda'\mathbf{k}''} \\
&= c_{\alpha,\mathbf{k}+\mathbf{q}}^\dagger c_{\beta,\mathbf{k}'-\mathbf{q}}^\dagger c_{\gamma,\mathbf{k}} \delta_{\lambda,\delta} \delta_{\mathbf{k}',\mathbf{k}''} c_{\lambda'\mathbf{k}''} - c_{\alpha,\mathbf{k}+\mathbf{q}}^\dagger c_{\beta,\mathbf{k}'-\mathbf{q}}^\dagger \delta_{\lambda\gamma} \delta_{\mathbf{k}\mathbf{k}''} c_{\delta,\mathbf{k}'} c_{\lambda'\mathbf{k}''} + \cancel{c_{\alpha,\mathbf{k}+\mathbf{q}}^\dagger c_{\beta,\mathbf{k}'-\mathbf{q}}^\dagger c_{\lambda\mathbf{k}''}^\dagger c_{\gamma,\mathbf{k}\delta,\mathbf{k}'} c_{\lambda'\mathbf{k}''}} \\
&\bullet \quad c_{\lambda\mathbf{k}''}^\dagger c_{\lambda'\mathbf{k}''} c_{\alpha,\mathbf{k}+\mathbf{q}}^\dagger c_{\beta,\mathbf{k}'-\mathbf{q}}^\dagger c_{\gamma,\mathbf{k}\delta,\mathbf{k}'} = c_{\lambda\mathbf{k}''}^\dagger \delta_{\lambda',\alpha} \delta_{\mathbf{k}'',\mathbf{k}+\mathbf{q}} c_{\beta,\mathbf{k}'-\mathbf{q}}^\dagger c_{\gamma,\mathbf{k}\delta,\mathbf{k}'} - c_{\lambda\mathbf{k}''}^\dagger c_{\alpha,\mathbf{k}+\mathbf{q}}^\dagger c_{\lambda'\mathbf{k}''} c_{\beta,\mathbf{k}'-\mathbf{q}}^\dagger c_{\gamma,\mathbf{k}\delta,\mathbf{k}'} \\
&= c_{\lambda\mathbf{k}''}^\dagger \delta_{\lambda',\alpha} \delta_{\mathbf{k}'',\mathbf{k}+\mathbf{q}} c_{\beta,\mathbf{k}'-\mathbf{q}}^\dagger c_{\gamma,\mathbf{k}\delta,\mathbf{k}'} - c_{\lambda\mathbf{k}''}^\dagger c_{\alpha,\mathbf{k}+\mathbf{q}}^\dagger \delta_{\lambda'\beta} \delta_{\mathbf{k}'',\mathbf{k}'-\mathbf{q}} c_{\gamma,\mathbf{k}\delta,\mathbf{k}'} + \cancel{c_{\lambda\mathbf{k}''}^\dagger c_{\alpha,\mathbf{k}+\mathbf{q}}^\dagger c_{\beta,\mathbf{k}'-\mathbf{q}}^\dagger c_{\lambda'\mathbf{k}''} c_{\gamma,\mathbf{k}\delta,\mathbf{k}'}} \\
[H^{Coulomb}, c_{\lambda\mathbf{k}''}^\dagger c_{\lambda'\mathbf{k}''}] &= \sum_{\mathbf{k},\mathbf{k}',\mathbf{q}} \sum_{\alpha\beta\gamma\delta} W_{\mathbf{k},\mathbf{k}',\mathbf{q}}^{\alpha\beta\gamma\delta} (c_{\alpha,\mathbf{k}+\mathbf{q}}^\dagger c_{\beta,\mathbf{k}'-\mathbf{q}}^\dagger c_{\gamma,\mathbf{k}} \delta_{\lambda,\delta} \delta_{\mathbf{k}',\mathbf{k}''} c_{\lambda'\mathbf{k}''} - c_{\alpha,\mathbf{k}+\mathbf{q}}^\dagger c_{\beta,\mathbf{k}'-\mathbf{q}}^\dagger \delta_{\lambda\gamma} \delta_{\mathbf{k}\mathbf{k}''} c_{\delta,\mathbf{k}'} c_{\lambda'\mathbf{k}''} \\
&\quad - c_{\lambda\mathbf{k}''}^\dagger \delta_{\lambda',\alpha} \delta_{\mathbf{k}'',\mathbf{k}+\mathbf{q}} c_{\beta,\mathbf{k}'-\mathbf{q}}^\dagger c_{\gamma,\mathbf{k}\delta,\mathbf{k}'} + c_{\lambda\mathbf{k}''}^\dagger c_{\alpha,\mathbf{k}+\mathbf{q}}^\dagger \delta_{\lambda'\beta} \delta_{\mathbf{k}'',\mathbf{k}'-\mathbf{q}} c_{\gamma,\mathbf{k}\delta,\mathbf{k}'})
\end{aligned}$$

$$\begin{aligned}
&= \sum_{\mathbf{k}, \mathbf{k}', \mathbf{q}} \sum_{\alpha \beta \gamma \delta} W_{\mathbf{k}, \mathbf{k}', \mathbf{q}}^{\alpha \beta \gamma \delta} c_{\alpha, \mathbf{k}+\mathbf{q}}^\dagger c_{\beta, \mathbf{k}'-\mathbf{q}}^\dagger c_{\gamma, \mathbf{k}} \delta_{\lambda, \delta} \delta_{\mathbf{k}', \mathbf{k}''} c_{\lambda' \mathbf{k}''} - \sum_{\mathbf{k}, \mathbf{k}', \mathbf{q}} \sum_{\alpha \beta \gamma \delta} W_{\mathbf{k}, \mathbf{k}', \mathbf{q}}^{\alpha \beta \gamma \delta} c_{\alpha, \mathbf{k}+\mathbf{q}}^\dagger c_{\beta, \mathbf{k}'-\mathbf{q}}^\dagger \delta_{\lambda \gamma} \delta_{\mathbf{k} \mathbf{k}''} c_{\delta, \mathbf{k}'} c_{\lambda' \mathbf{k}''} \\
&- \sum_{\mathbf{k}, \mathbf{k}', \mathbf{q}} \sum_{\alpha \beta \gamma \delta} W_{\mathbf{k}, \mathbf{k}', \mathbf{q}}^{\alpha \beta \gamma \delta} c_{\lambda \mathbf{k}''}^\dagger \delta_{\lambda', \alpha} \delta_{\mathbf{k}'', \mathbf{k}+\mathbf{q}} c_{\beta, \mathbf{k}'-\mathbf{q}}^\dagger c_{\gamma, \mathbf{k}} c_{\delta, \mathbf{k}'} + \sum_{\mathbf{k}, \mathbf{k}', \mathbf{q}} \sum_{\alpha \beta \gamma \delta} W_{\mathbf{k}, \mathbf{k}', \mathbf{q}}^{\alpha \beta \gamma \delta} c_{\lambda \mathbf{k}''}^\dagger c_{\alpha, \mathbf{k}+\mathbf{q}}^\dagger \delta_{\lambda' \beta} \delta_{\mathbf{k}'', \mathbf{k}'-\mathbf{q}} c_{\gamma, \mathbf{k}} c_{\delta, \mathbf{k}'} \\
&= \sum_{\mathbf{k}, \mathbf{q}} \sum_{\alpha \beta \gamma} W_{\mathbf{k}, \mathbf{k}'', \mathbf{q}}^{\alpha \beta \gamma \lambda} c_{\alpha, \mathbf{k}+\mathbf{q}}^\dagger c_{\beta, \mathbf{k}''-\mathbf{q}}^\dagger c_{\gamma, \mathbf{k}} c_{\lambda' \mathbf{k}''} - \sum_{\mathbf{k}'', \mathbf{k}', \mathbf{q}} \sum_{\alpha \beta \delta} W_{\mathbf{k}'', \mathbf{k}', \mathbf{q}}^{\alpha \beta \lambda \delta} c_{\alpha, \mathbf{k}''+\mathbf{q}}^\dagger c_{\beta, \mathbf{k}'-\mathbf{q}}^\dagger c_{\delta, \mathbf{k}'} c_{\lambda' \mathbf{k}''} \\
&- \sum_{\mathbf{k}', \mathbf{q}} \sum_{\beta \gamma \delta} W_{\mathbf{k}'', \mathbf{k}', \mathbf{q}}^{\lambda' \beta \gamma \delta} c_{\lambda \mathbf{k}''}^\dagger c_{\beta, \mathbf{k}'-\mathbf{q}}^\dagger c_{\gamma, \mathbf{k}''-\mathbf{q}} c_{\delta, \mathbf{k}'} + \sum_{\mathbf{k}, \mathbf{q}} \sum_{\alpha \gamma \delta} W_{\mathbf{k}, \mathbf{k}', \mathbf{q}}^{\alpha \lambda' \gamma \delta} c_{\lambda \mathbf{k}''}^\dagger c_{\alpha, \mathbf{k}+\mathbf{q}}^\dagger c_{\gamma, \mathbf{k}} c_{\delta, \mathbf{k}''+\mathbf{q}} \\
&= \sum_{\mathbf{k}, \mathbf{q}} \sum_{\alpha \beta \gamma} W_{\mathbf{k}, \mathbf{k}'', \mathbf{q}}^{\alpha \beta \gamma \lambda} c_{\alpha, \mathbf{k}+\mathbf{q}}^\dagger c_{\beta, \mathbf{k}''-\mathbf{q}}^\dagger c_{\gamma, \mathbf{k}} c_{\lambda' \mathbf{k}''} - \sum_{\mathbf{k}'', \mathbf{k}', \mathbf{q}} \sum_{\alpha \beta \delta} W_{\mathbf{k}'', \mathbf{k}', \mathbf{q}}^{\alpha \beta \lambda \delta} c_{\alpha, \mathbf{k}''+\mathbf{q}}^\dagger c_{\beta, \mathbf{k}'-\mathbf{q}}^\dagger c_{\delta, \mathbf{k}'} c_{\lambda' \mathbf{k}''} \\
&- \sum_{\mathbf{k}', \mathbf{q}} \sum_{\beta \gamma \delta} W_{\mathbf{k}'', \mathbf{k}', \mathbf{q}}^{\lambda' \beta \gamma \delta} c_{\lambda \mathbf{k}''}^\dagger c_{\beta, \mathbf{k}'-\mathbf{q}}^\dagger c_{\gamma, \mathbf{k}''-\mathbf{q}} c_{\delta, \mathbf{k}'} + \sum_{\mathbf{k}, \mathbf{q}} \sum_{\alpha \gamma \delta} W_{\mathbf{k}, \mathbf{k}', \mathbf{q}}^{\alpha \lambda' \gamma \delta} c_{\lambda \mathbf{k}''}^\dagger c_{\alpha, \mathbf{k}+\mathbf{q}}^\dagger c_{\gamma, \mathbf{k}} c_{\delta, \mathbf{k}''+\mathbf{q}} \\
&= 2 \sum_{\mathbf{k}' \mathbf{q}} \left(\sum_{\alpha \beta \gamma} W_{\mathbf{k}'', \mathbf{k}', \mathbf{q}}^{\alpha \beta \gamma \lambda} c_{\alpha \mathbf{k}''+\mathbf{q}}^\dagger c_{\beta \mathbf{k}'-\mathbf{q}}^\dagger c_{\gamma \mathbf{k}'} c_{\lambda' \mathbf{k}''} + W_{\mathbf{k}', \mathbf{k}''+\mathbf{q}, \mathbf{q}}^{\alpha \lambda' \gamma \delta} c_{\lambda \mathbf{k}''}^\dagger c_{\alpha \mathbf{k}'+\mathbf{q}}^\dagger c_{\gamma \mathbf{k}''+\mathbf{q}} c_{\delta \mathbf{k}'} \right) \quad (65)
\end{aligned}$$

Using the random phase approximation and factorization to split the 4-operators term into the products of 2-operators term (Hartree-Fock approximation):

$$\begin{aligned}
\sum_{\mathbf{k}' \mathbf{q}} \left\langle c_{\alpha \mathbf{k}''+\mathbf{q}}^\dagger c_{\beta \mathbf{k}'-\mathbf{q}}^\dagger c_{\gamma \mathbf{k}'} c_{\lambda' \mathbf{k}''} \right\rangle &= - \sum_{\mathbf{k}' \mathbf{q}} \left\langle c_{\alpha \mathbf{k}''+\mathbf{q}}^\dagger c_{\gamma \mathbf{k}'} \right\rangle \left\langle c_{\beta \mathbf{k}'-\mathbf{q}}^\dagger c_{\lambda' \mathbf{k}''} \right\rangle \delta_{\mathbf{k}' \mathbf{k}''+\mathbf{q}} \\
&= - \sum_{\mathbf{q}} \left\langle c_{\alpha \mathbf{k}''+\mathbf{q}}^\dagger c_{\gamma \mathbf{k}''+\mathbf{q}} \right\rangle \left\langle c_{\mathbf{k}''}^\dagger c_{\lambda' \mathbf{k}''} \right\rangle \quad (66)
\end{aligned}$$

$$\begin{aligned}
\sum_{\mathbf{k}' \mathbf{q}} \left\langle c_{\lambda \mathbf{k}''}^\dagger c_{\alpha \mathbf{k}'+\mathbf{q}}^\dagger c_{\gamma \mathbf{k}''+\mathbf{q}} c_{\delta \mathbf{k}'} \right\rangle &= \sum_{\mathbf{k}' \mathbf{q}} \left\langle c_{\lambda \mathbf{k}''}^\dagger c_{\delta \mathbf{k}'} \right\rangle \left\langle c_{\alpha \mathbf{k}'+\mathbf{q}}^\dagger c_{\gamma \mathbf{k}''+\mathbf{q}} \right\rangle \delta_{\mathbf{k}', \mathbf{k}''} \\
&= \sum_{\mathbf{q}} \left\langle c_{\lambda \mathbf{k}''}^\dagger c_{\delta \mathbf{k}''} \right\rangle \left\langle c_{\alpha \mathbf{k}''+\mathbf{q}}^\dagger c_{\gamma \mathbf{k}''+\mathbf{q}} \right\rangle \quad (67)
\end{aligned}$$

Include Eqs. (66) and (67) into Eq. (65). Including all the communication term in Eqs. (63), (64) and (65) into Eq. (40) to get the SBE in Hartree-Fock approximation:

$$\begin{aligned}
\frac{d}{dt} \rho_{\lambda \lambda'}(\mathbf{k}) &= -\frac{i}{\hbar} (\varepsilon_{\lambda}(\mathbf{k}) - \varepsilon_{\lambda'}(\mathbf{k})) \rho_{\lambda \lambda'} - \frac{ie}{\hbar m} \mathbf{A}(t) \sum_{\mu} (\mathbf{p}_{\lambda \mu}(\mathbf{k}) \rho_{\mu \lambda'}(\mathbf{k}) - \rho_{\lambda \mu}(\mathbf{k}) \mathbf{p}_{\mu \lambda'}(\mathbf{k})) \\
&\quad + \frac{i}{\hbar} (\Omega_{\lambda \mu}(\mathbf{k}) \rho_{\mu \lambda'}(\mathbf{k}) - \rho_{\lambda \mu}(\mathbf{k}) \Omega_{\mu \lambda'}(\mathbf{k})) \quad (68)
\end{aligned}$$

C Dipole Matrix Elements

We have the position matrix element:

$$\langle \psi_{\lambda \mathbf{k}} | \mathbf{r} | \psi_{\lambda' \mathbf{k}'} \rangle = \int \frac{d^3 r}{V} u_{\lambda \mathbf{k}}^*(\mathbf{r}) e^{-i\mathbf{k} \cdot \mathbf{r}} \mathbf{r} u_{\lambda' \mathbf{k}'}(\mathbf{r}) e^{i\mathbf{k}' \cdot \mathbf{r}} \quad (69)$$

$$\begin{aligned} &= i \nabla_{\mathbf{k}} \left(\int \frac{d^3 r}{V} e^{-i\mathbf{k} \cdot \mathbf{r}} u_{\lambda \mathbf{k}}^*(\mathbf{r}) u_{\lambda' \mathbf{k}'}(\mathbf{r}) e^{i\mathbf{k}' \cdot \mathbf{r}} \right) - \int \frac{d^3 r}{V} i e^{-i\mathbf{k} \cdot \mathbf{r}} (\nabla_{\mathbf{k}} u_{\lambda \mathbf{k}}^*) u_{\lambda' \mathbf{k}'} e^{i\mathbf{k}' \cdot \mathbf{r}} \\ &= i \nabla_{\mathbf{k}} \left(\frac{1}{N} \sum_i^N e^{i(\mathbf{k}' - \mathbf{k}) \cdot \mathbf{R}_i} \int_{V_{cell}} \frac{d^3 r}{V_{cell}} e^{-i\mathbf{k} \cdot \mathbf{r}} u_{\lambda \mathbf{k}}^*(\mathbf{r}) u_{\lambda' \mathbf{k}'}(\mathbf{r}) e^{i\mathbf{k}' \cdot \mathbf{r}} \right) \\ &\quad - i \frac{1}{N} \sum_i^N e^{i(\mathbf{k}' - \mathbf{k}) \cdot \mathbf{R}_i} \int_{V_{cell}} \frac{d^3 r}{V_{cell}} e^{i(\mathbf{k}' - \mathbf{k}) \cdot \mathbf{r}} (\nabla_{\mathbf{k}} u_{\lambda \mathbf{k}}^*) u_{\lambda' \mathbf{k}'}. \end{aligned} \quad (70)$$

Applying the long-wave-length approximation to have

$$\langle \psi_{\lambda \mathbf{k}} | \mathbf{r} | \psi_{\lambda' \mathbf{k}'} \rangle \approx i \nabla_{\mathbf{k}} \delta_{\mathbf{k}, \mathbf{k}'} \delta_{\lambda \lambda'} - i \delta_{\mathbf{k}, \mathbf{k}'} \langle \nabla_{\mathbf{k}} u_{\lambda \mathbf{k}} | u_{\lambda' \mathbf{k}'} \rangle, \quad (71)$$

The dielectric matrix elements are defined as:

$$\xi_{\lambda \lambda'}(\mathbf{k}) = -i \langle \nabla_{\mathbf{k}} u_{\lambda \mathbf{k}} | u_{\lambda' \mathbf{k}'} \rangle, \quad (72)$$

Include Eq. (72) into Eq. (71) to have

$$\langle \psi_{\lambda \mathbf{k}} | \mathbf{r} | \psi_{\lambda' \mathbf{k}'} \rangle = \delta_{\mathbf{k}, \mathbf{k}'} (i \delta_{\lambda \lambda'} \nabla_{\mathbf{k}} + \xi_{\lambda \lambda'}(\mathbf{k})), \quad (73)$$

Using Eqs. (73), (32) and the relation $[H_{1e}^0, \mathbf{r}] = -i \frac{\hbar}{m} \mathbf{p}$ for $\lambda \neq \lambda'$ to get:

$$\xi_{\lambda \lambda'}(\mathbf{k}) = -\frac{i \hbar}{m} \frac{\mathbf{p}_{\lambda \lambda'}(\mathbf{k})}{\varepsilon_{\lambda}(\mathbf{k}) - \varepsilon_{\lambda'}(\mathbf{k})} \quad (74)$$

References

- [1] Jie Jiang, Zhizhong Chen, Yang Hu, Yu Xiang, Lifu Zhang, Yiping Wang, Gwo-Ching Wang, and Jian Shi. Flexo-photovoltaic effect in MoS₂. *Nat. Nanotechnol.*, 16(8):894–901, August 2021. Publisher: Nature Publishing Group.
- [2] William Shockley and Hans J. Queisser. Detailed Balance Limit of Efficiency of p-n Junction Solar Cells. *Journal of Applied Physics*, 32(3):510–519, March 1961.
- [3] B. I. Sturman. Ballistic and shift currents in the bulk photovoltaic effect theory. *Phys.-Usp.*, 63(4):407, April 2020. Publisher: IOP Publishing.
- [4] A. K. Geim and I. V. Grigorieva. Van der Waals heterostructures. *Nature*, 499(7459):419–425, July 2013. Publisher: Nature Publishing Group.
- [5] Qing Hua Wang, Kourosh Kalantar-Zadeh, Andras Kis, Jonathan N. Coleman, and Michael S. Strano. Electronics and optoelectronics of two-dimensional transition metal dichalcogenides. *Nature Nanotech.*, 7(11):699–712, November 2012.
- [6] Di Xiao, Wang Yao, and Qian Niu. Valley-Contrasting Physics in Graphene: Magnetic Moment and Topological Transport. *Phys. Rev. Lett.*, 99(23):236809, December 2007. Publisher: American Physical Society.
- [7] Wang Yao, Di Xiao, and Qian Niu. Valley-dependent optoelectronics from inversion symmetry breaking. *Phys. Rev. B*, 77(23):235406, June 2008. Publisher: American Physical Society.
- [8] Bumseop Kim, Noejung Park, and Jeongwoo Kim. Giant bulk photovoltaic effect driven by the wall-to-wall charge shift in WS₂ nanotubes. *Nat Commun*, 13(1):3237, June 2022. Publisher: Nature Publishing Group.
- [9] Y. J. Zhang, T. Ideue, M. Onga, F. Qin, R. Suzuki, A. Zak, R. Tenne, J. H. Smet, and Y. Iwasa. Enhanced intrinsic photovoltaic effect in tungsten disulfide nanotubes. *Nature*, 570(7761):349–353, June 2019. Publisher: Nature Publishing Group.
- [10] Dongyang Yang, Jingda Wu, Benjamin T. Zhou, Jing Liang, Toshiya Ideue, Teri Siu, Kashif Masud Awan, Kenji Watanabe, Takashi Taniguchi, Yoshihiro Iwasa, Marcel Franz, and Ziliang Ye. Spontaneous-polarization-induced photovoltaic effect in rhombohedrally stacked MoS₂. *Nat. Photon.*, 16(6):469–474, June 2022. Publisher: Nature Publishing Group.
- [11] E. V. Kirichenko and V. A. Stephanovich. The influence of Coulomb interaction screening on the excitons in disordered two-dimensional insulators. *Sci Rep*, 11(1):11956, June 2021. Number: 1 Publisher: Nature Publishing Group.

- [12] Changjian Zhang, Haining Wang, Weimin Chan, Christina Manolatou, and Farhan Rana. Absorption of light by excitons and trions in monolayers of metal dichalcogenide MoS_2 : Experiments and theory. *Phys. Rev. B*, 89(20):205436, May 2014. Publisher: American Physical Society.
- [13] Ashwin Ramasubramaniam. Large excitonic effects in monolayers of molybdenum and tungsten dichalcogenides. *Phys. Rev. B*, 86(11):115409, September 2012. Publisher: American Physical Society.
- [14] Diana Y. Qiu, Felipe H. da Jornada, and Steven G. Louie. Optical Spectrum of MoS_2 : Many-Body Effects and Diversity of Exciton States. *Phys. Rev. Lett.*, 111(21):216805, November 2013. Publisher: American Physical Society.
- [15] Tawinan Cheiwchanchamnangij and Walter R. L. Lambrecht. Quasiparticle band structure calculation of monolayer, bilayer, and bulk MoS_2 . *Phys. Rev. B*, 85(20):205302, May 2012. Publisher: American Physical Society.
- [16] Hongliang Shi, Hui Pan, Yong-Wei Zhang, and Boris I. Yakobson. Quasiparticle band structures and optical properties of strained monolayer MoS_2 and WS_2 . *Phys. Rev. B*, 87(15):155304, April 2013. Publisher: American Physical Society.
- [17] Chendong Zhang, Amber Johnson, Chang-Lung Hsu, Lain-Jong Li, and Chih-Kang Shih. Direct imaging of band profile in single layer MoS_2 on graphite: Quasiparticle energy gap, metallic edge states, and edge band bending. *Nano Letters*, 14(5):2443–2447, 2014. PMID: 24783945.
- [18] L. Meckbach, J. Hader, U. Huttner, J. Neuhaus, J. T. Steiner, T. Stroucken, J. V. Moloney, and S. W. Koch. Ultrafast band-gap renormalization and build-up of optical gain in monolayer MoTe_2 . *Phys. Rev. B*, 101(7):075401, February 2020.
- [19] Timothy C. Berkelbach, Mark S. Hybertsen, and David R. Reichman. Theory of neutral and charged excitons in monolayer transition metal dichalcogenides. *Phys. Rev. B*, 88(4):045318, July 2013.
- [20] Gui-Bin Liu, Wen-Yu Shan, Yugui Yao, Wang Yao, and Di Xiao. Three-band tight-binding model for monolayers of group-VIB transition metal dichalcogenides. *Phys. Rev. B*, 88(8):085433, August 2013. Publisher: American Physical Society.
- [21] Di Xiao, Gui-Bin Liu, Wanxiang Feng, Xiaodong Xu, and Wang Yao. Coupled Spin and Valley Physics in Monolayers of MoS_2 and Other Group-VI Dichalcogenides. *Phys. Rev. Lett.*, 108(19):196802, May 2012. Publisher: American Physical Society.
- [22] L. F. Mattheiss. Band Structures of Transition-Metal-Dichalcogenide Layer Compounds. *Phys. Rev. B*, 8(8):3719–3740, October 1973. Publisher: American Physical Society.

- [23] S. Lebègue and O. Eriksson. Electronic structure of two-dimensional crystals from ab initio theory. *Phys. Rev. B*, 79(11):115409, March 2009. Publisher: American Physical Society.
- [24] Z. Y. Zhu, Y. C. Cheng, and U. Schwingenschlögl. Giant spin-orbit-induced spin splitting in two-dimensional transition-metal dichalcogenide semiconductors. *Phys. Rev. B*, 84(15):153402, October 2011. Publisher: American Physical Society.
- [25] C. Ataca, H. Şahin, and S. Ciraci. Stable, Single-Layer MX₂ Transition-Metal Oxides and Dichalcogenides in a Honeycomb-Like Structure. *J. Phys. Chem. C*, 116(16):8983–8999, April 2012. Publisher: American Chemical Society.
- [26] Haining Wang, Changjian Zhang, and Farhan Rana. Ultrafast dynamics of defect-assisted electron–hole recombination in monolayer mos₂. *Nano Letters*, 15(1):339–345, 2015. PMID: 25546602.
- [27] Hartmut Haug and Stephan W. Koch. *Quantum Theory Of The Optical And Electronic Properties Of Semiconductors (fifth Edition)*. World Scientific Publishing Company, January 2009. Google-Books-ID: 1J1IDQAAQBAJ.
- [28] Chendong Zhang, Amber Johnson, Chang-Lung Hsu, Lain-Jong Li, and Chih-Kang Shih. Direct Imaging of Band Profile in Single Layer MoS₂ on Graphite: Quasiparticle Energy Gap, Metallic Edge States, and Edge Band Bending. *Nano Lett.*, 14(5):2443–2447, May 2014. Publisher: American Chemical Society.
- [29] D. Erben, A. Steinhoff, C. Gies, G. Schönhoff, T. O. Wehling, and F. Jahnke. Excitation-induced transition to indirect band gaps in atomically thin transition-metal dichalcogenide semiconductors. *Phys. Rev. B*, 98(3):035434, July 2018.
- [30] D. Erben, A. Steinhoff, M. Lorke, and F. Jahnke. Optical nonlinearities in the excited carrier density of atomically thin transition metal dichalcogenides. *Phys. Rev. B*, 106(4):045409, July 2022.
- [31] Chau Duc Phuong Vo and Thanh Duc Huynh. Calculation of shift current tensors in two-dimensional transition metal dichalcogenides. *E3S Web Conf.*, 496:02002, 2024. Publisher: EDP Sciences.